ACS OMEGA

http://pubs.acs.org/journal/acsodf

Article

Numerical Investigation and Response Surface Optimization of the Effective Modulus and Electrical and Thermal Conductivities of the Borophene Nanoplatelet-Reinforced PEDOT:PSS Nanocomposite for Energy Storage Application

Gbolahan Joseph Adekoya, Oluwasegun Chijioke Adekoya, Rotimi Emmanuel Sadiku, Yskandar Hamam, and Suprakas Sinha Ray*

Cite This: *ACS Omega* 2022, 7, 48447−48466

Read Online

ACCESS | Metrics & More | Article Recommendations | Supporting Information

ABSTRACT: Conductive organic nanocomposites have been widely employed to achieve a variety of purposes, particularly for energy storage applications, making it necessary to investigate transport properties such as electron and heat transport qualities based on geometric shapes and component materials. Due to the solid B−B bonds, unique atomic structure, and energy storage potential, borophene has received significant attention due to its reported ultrahigh mechanical modulus and metallic conduction. Herein, we investigated the effect and interaction of content materials (volume fraction) and geometric parameters such as the aspect ratio and orientation of borophene nanoplatelet (BNP) inclusions on the mechanical integrity and transport features (electrical and thermal conductivities) of a poly(3,4-ethylene dioxythiophene):poly(4-styrene sulfonate) (PEDOT:PSS) electrode. The boundary condition is crucial in developing the predictive models for the optimized mechanical and transport properties of the composites. The effective modulus, electrical conductivity, and thermal conductivity of the BNP-reinforced PEDOT:PSS-based nanocomposite are evaluated using the periodic boundary condition, the representative volume element-based finite element homogenization, and statistical analysis response surface techniques. The optimal parameters for the PEDOT:PSS/BNP nanocomposite for energy storage application are predicted based on the desirability function to have a 13.96% volume fraction of BNPs, having an aspect ratio of 0.04 at 45° inclination. The desirability value achieved for the material hinges was 0.78 with a predicted Young's modulus of 6.73 GPa, the electrical conductivity was 633.85 S/cm, and the thermal conductivity was 1.96 W/m K at a generally high predictive performance of <0.03 error. The effective thermal conductivity of the nanocomposite was determined by considering Kapitsa nanoeffects, which exhibit an interfacial thermal resistance of 2.42×10^{-9} m^2 K/W. Based on these improved findings, the enhanced PEDOT:PSS/BNP nanocomposite electrode would be a promising material for metal-ion batteries.

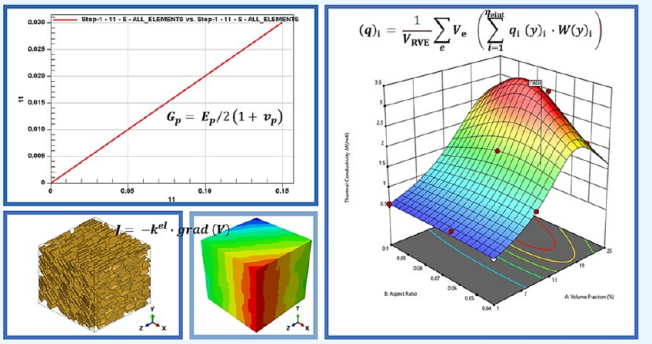

1. INTRODUCTION

The increasing expansion of wearable and portable devices has raised research interest in flexible energy storage systems with the best performance.[1,2] In this direction, polymers have a crucial role in developing efficient, reliable, and environmentally friendly electrochemical power sources.[3] Electrically conductive and thermally stable materials are necessary for the correct operation of energy storage devices.[4,5] As such, the emphasis of the ongoing research is on polymeric materials for electrochemical power devices that possess good stability and conductivity and are affordable. Energy conversion and storage applications for polymer and polymeric composite materials with customizable characteristics have been investigated.[6] Among these materials, conductive polymers, such as poly(3,4-ethylene dioxythiophene):poly(4-styrene sulfonate) (PEDOT:PSS),[7−10] have been widely researched for energy storage applications for their more extensive range of tunable electrical conductivity, higher mechanical stability, general accessibility, less weight in comparison to that of other materials, and ease of processing.[11,12] More importantly, PEDOT:PSS-based conductive nanocomposites are suitable materials for a variety of purposes, specifically for supercapacitor and battery applications because they have superior electrochemical activities, more

Received: October 18, 2022
Accepted: November 15, 2022
Published: December 13, 2022

surface area, and higher electrical conductivity than bulk polymers.[13−15] Varghese and colleagues demonstrated using Co_3O_4 nanoparticles coated with a conducting polymer (PEDOT:PSS) as the anode for applications involving sodium-ion batteries.[16] Meanwhile, to improve the specific capacitance and rate performance of graphene-based fiber-shaped supercapacitors, Teng and colleagues developed a hierarchically porous reduced graphene oxide/PEDOT:PSS hybrid fiber by the combined confined growth and acid treatment strategy.[17] In recent studies, several nanomaterials have been experimentally employed with PEDOT:PSS for energy storage, among which an intriguing nanomaterial is the 2D boron sheet.[18]

Due to its anisotropic atomic structure, borophene has exceptional anisotropic mechanical, electrical, optical, and thermal capabilities. In addition, borophene exhibits metallic properties and a buckled shape, which makes it an excellent material for energy storage devices. It offers an advanced alternative nanomaterial for flexible nanoelectronics due to its low mass density, good tensile strength, and intrinsic phonon-mediated superconductivity. Borophene is a desirable anode material for ion batteries since it has the largest storage capacity among 2D materials, which is significantly greater than that of the graphite electrode.[19−25] According to experimental research, borophene possesses in-plane elastic moduli of 586.2 and 1372.4 GPa, with matching thicknesses of 0.27−0.31 nm in the zigzag and armchair directions, respectively.[19,20] Meanwhile, the armchair and zigzag thermal conductivities of borophene are 92.0 and 86.3 W/m K at room temperature, respectively.[26] However, the reported freestanding multilayered borophene, a p-type semiconductor material, exhibited a very low electrical conductivity of 1.4×10^{-7} S/cm.[18] This presents an inherent challenge in using this wonder material as it is not practical to scale up its production without impairing its excellent properties.

As such, conducting experimental studies on nanocomposites requires careful planning, is costly, and takes a lot of time. Analytical and computational methods are intriguing to predict the properties of a composite. Many analytical techniques, such as the finite element (FE) analysis for calculating the elastic modulus of a two-phase composite and for computing effective electrical and thermal conductivities, may be utilized to understand better the physical behavior of materials at the atomic and subatomic levels.[27−29] It has been demonstrated that the most popular of these models are in good accord with the experimental data.[30,31] Besides, the additional use of the response surface approach enables a substantial decrease in the processing effort while still delivering accurate approximations. To design an approximate numerical homogenization process for inhomogeneous nonlinear porous materials, Beluch and Hatlas,[32] for instance, use response surfaces in the numerical homogenization.[32]

By creating a statistical response surface and FE computational model,[33,34] this study aims to analyze the properties of the borophene nanoplatelet (BNP)-reinforced PEDOT:PSS nanocomposite based on the experimentally reported data. This will provide the first insight into the type of composites being proposed, spur research, make practical applications easier for the development of energy storage electrodes, and offer guidance for the future design of similar composite materials. It has been reported that the properties of conductive polymers depend on the loading of conducting nanoparticles, filler aspect ratio (AR), and orientation of the dispersed/distributed nanoparticles in a polymer matrix.[35] Therefore, the mechanical integrity and transport characteristics (electrical and thermal conductivities) of the BNP-reinforced PEDOT:PSS nanocomposite electrode were examined in this study, as well as the impact and interaction of the content materials (volume fraction) and geometric parameters of BNP inclusions, such as the AR and orientation. Moreover, boundary conditions play a critical role in creating prediction models for the composites' optimal mechanical and transport characteristics. Therefore, using the periodic boundary condition, the representative volume element (RVE)-based FE homogenization, and statistical response surface approaches, the effective modulus, electrical conductivity, and thermal conductivity of the BNP-reinforced PEDOT:PSS-based nanocomposite are assessed.

2. NUMERICAL HOMOGENIZATION

To predict the effective elastic modulus and electrical and thermal conductivities of composites with discontinuous inclusions, the RVE-based FE homogenization approach is used in this work. An RVE is the smallest volume of the microstructure that contains all of the general qualities of the microstructure, including shape, size, volume fraction, and phase randomization.[36] The volume of the RVE is defined as V, given the RVE ω of the composites. If the matrix ω_m is composed of the volume of V_m and volume fraction of $\nu_m = V_m/V$ and the inclusion ω_f is made up of the volume of V_f and volume fraction of $\nu_f = 1 - \nu_m = V_f/V$), then ω_m and ω_f make up the RVE ω. The following average functions inside the RVE ω are specified for any micro-field μ.[37]

$$(\mu) = \frac{1}{V}\int_{\omega} \mu(x)\,\mathrm{d}x \text{ and } \langle\mu\rangle_{\omega_i} = \frac{1}{V_i}\int_{\omega_i} \mu(x)\,\mathrm{d}x, \quad \text{with } i = \mathrm{m}, \mathrm{f} \tag{1}$$

Subsequently, using Digimat software[38] and the design treatments produced by the RSM custom design, the realistic stochastic RVE of the PEDOT:PSS/BNP nanocomposite was developed. It should be big enough to include the essential microstructural characteristics while being compact enough to allow for a preliminary assessment of the micro-homogeneity field across the RVE.[39] Accordingly, the program automatically produced an RVE of $375 \times 375 \times 375$ nm^3 with 565 BNP inclusions for the optimum composites. A non-conforming (voxel) meshing type was used to mesh the RVE with automatic element size definition. As opposed to freestanding borophene peeled off in isopropyl alcohol, which had a thickness of 4.7 nm and a surface area of 1791 nm^2, and borophene stripped in dimethyl formamide, which had an average thickness of 1.8 nm and a surface area of 19 827 nm^2,[40] the average thickness used for this study is 3 nm with an AR ranging from 0.04 to 0.1. The volume fraction of the BNP inclusions ranges from 1 to 25%. Meanwhile, the orientation of the inclusion is investigated across three factor levels, namely, at 45°, random, and 90°.

The elastic modulus of the nanocomposite was calculated using transversely isotropic elasticity due to the anisotropic characteristics of borophene around its axis. Transverse isotropy, a unique subclass of orthotropy, is defined by a plane of isotropy at every point in the substance. Transverse isotropy necessitates that assuming the 1−2 plane to be the plane of isotropy at every point,

https://doi.org/10.1021/acsomega.2c06716
ACS Omega 2022, 7, 48447−48466

$$E_1 = E_2 = E_p$$
$$\nu_{31} = \nu_{32} = \nu_{tp}$$
$$\nu_{13} = \nu_{23} = \nu_{pt}$$
$$G_{13} = G_{23} = G_t \quad (2)$$

where p and t stand for "in-plane" and "transverse," respectively.

As a result, while ν_{tp} has the Poisson's ratio physical meaning that describes the strain caused by stress normal to it in the plane of isotropy, ν_{pt} describes the transverse strain induced by stress in the plane of isotropy in the direction normal to that plane. For the most part, ν_{tp} and ν_{pt} are not equivalent and are connected by $\nu_{tp}/E_t = \nu_{pt}/E_p$. As a result of the stress−strain laws

$$\begin{Bmatrix} \varepsilon_{11} \\ \varepsilon_{22} \\ \varepsilon_{33} \\ \gamma_{12} \\ \gamma_{13} \\ \gamma_{23} \end{Bmatrix} = \begin{bmatrix} 1/E_p & -\nu_p/E_p & -\nu_{tp}/E_t & 0 & 0 & 0 \\ -\nu_p/E_p & 1/E_p & -\nu_{tp}/E_t & 0 & 0 & 0 \\ -\nu_{pt}/E_p & -\nu_{pt}/E_p & 1/E_t & 0 & 0 & 0 \\ 0 & 0 & 0 & 1/G_p & 0 & 0 \\ 0 & 0 & 0 & 0 & 1/G_t & 0 \\ 0 & 0 & 0 & 0 & 0 & 1/G_t \end{bmatrix} \begin{Bmatrix} \sigma_{11} \\ \sigma_{22} \\ \sigma_{33} \\ \sigma_{12} \\ \sigma_{13} \\ \sigma_{23} \end{Bmatrix} \quad (3)$$

where $G_p = E_p/2(1 + \nu_p)$ and there are only five independent constants in total. The stability relations for orthotropic elasticity in the transversely isotropic case reduce to

$$E_p, E_t, G_p, G_t > 0$$
$$|\nu_{pt}| < 1$$
$$|\nu_{pt}| < (E_p/E_t)^{1/2}$$
$$|\nu_{tp}| < (E_t/E_p)^{1/2}$$
$$1 - \nu_p^2 - 2\nu_{pt}\nu_{tp} - 2\nu_p\nu_{pt}\nu_{tp} > 0$$

The electrical conductivity of the nanocomposite was calculated using isotropic conditions due to the reported electrical conductivity for borophene and PEDOT:PSS in ref 18. Ohm's law relates the gradient of potential to a flux, which is in this case, the electric potential (EPOT) V and the current density J

$$J = -k^{el} \cdot \text{grad}\,(V) \quad (4)$$

with the electrical conductivity matrix, k^{el}, which can be

$$k^{el} = k \begin{bmatrix} 1 & 0 & 0 \\ 0 & 1 & 0 \\ 0 & 0 & 1 \end{bmatrix} \quad (5)$$

In composite materials, the percolation phenomena are mostly seen during electrical conduction. It has been found through experimental observation that the electrical conductivity of a composite reinforced with conductive inclusions substantially relies on the volume percentage of inclusion. For low-volume fractions, the conductivity of the matrix dominates the electrical conductivity of the composite. When the volume percentage approaches a certain threshold, it is noticed that the conductivity of the composites increases by many orders of magnitude for greater volume fractions of inclusions. The materials and inclusion's shape affect this limit, known as the percolation threshold.[35] The emergence of "percolating clusters," or groupings of inclusions that are in electrical contact (i.e., touching each other or near enough for an electron to hop from one inclusion to the next—electron tunneling), is what causes this significant increase in the conductivity of the composite.[38]

Moreover, poor thermal transfer qualities make thermal management of batteries with high energy densities and charge rates difficult. The heat resistance of a battery with a low k increases noticeably as it becomes thicker for increasing capacity. When there is a lot of heat generation, inefficient thermal transport prevents effective heat dissipation, increasing battery temperature, and a wide temperature range within the cell. The significant temperature differential may result in various degrees of electrode use and, thus, variable ageing rates, which ultimately speeds up the ageing of batteries. In a worst case scenario, the unfavorable temperature increase might result in thermal runaway and SEI disintegration. The battery thermal safety issues can be reduced by enhancing the thermal transfer qualities inside batteries.[45] The PEDOT:PSS and BNP thermal conductivities are transversely isotropic along their axis. The following heat conduction equation, derived from the first law of thermodynamics (commonly known as the conservation of energy), must be valid for every material point x within the RVE ω.

$$\rho(x)\cdot c(x)\cdot \frac{\partial \boldsymbol{T}(\boldsymbol{x})}{\partial \boldsymbol{t}} + \text{div}(\boldsymbol{q}(\boldsymbol{x})) - Q(x) = 0 \quad (6)$$

where the material point x's density and specific heat are denoted by $\rho(x)$ and $c(x)$, respectively. The temperature and heat flux at the material point x are $\boldsymbol{T}(\boldsymbol{x})$ and $\boldsymbol{q}(\boldsymbol{x})$, respectively. The rate at which the material point x generates internal energy per unit volume is known as $\boldsymbol{Q}(\boldsymbol{x})$. Fourier's law[46,47] may be used to represent the heat flux $\boldsymbol{q}(\boldsymbol{x})$ as

$$q(x) = -k(x) \bullet \nabla \boldsymbol{T}(\text{x}) \quad (7)$$

where k denotes the material's thermal conductivity at position x. Considering the ensuing boundary conditions and combining with eq 8

$$T(x) = \overline{\boldsymbol{T}}(\boldsymbol{x}) \text{ on } \partial\boldsymbol{\Omega}_{\boldsymbol{T}} \text{ and } q(x) = \overline{\boldsymbol{q}}(\boldsymbol{x}) \text{ on } \partial\boldsymbol{\Omega}_{\boldsymbol{q}} \quad (8)$$

it is possible to solve the heat flux $\boldsymbol{q}(\boldsymbol{x})$ and temperature $\boldsymbol{T}(\boldsymbol{x})$ of any material point x inside the RVE x. The temperature and heat flux fields in the RVE x may be significantly impacted by boundary conditions as well as internal heat production. The effective thermal conductivity, however, is a property of the materials and should not be affected by such outside factors. Consequently, the steady-state heat transfer with the specified temperature boundary condition is considered to determine the RVE's effective thermal conductivity

$$\text{div}(\boldsymbol{k}\cdot\nabla\boldsymbol{T}) = 0 \text{ with } T = \overline{\boldsymbol{T}} \text{ on} \partial\Omega_T \quad (9)$$

The heat flux $\boldsymbol{q}(\boldsymbol{x})$ and temperature $\boldsymbol{T}(\boldsymbol{x})$ of any material point x inside the RVE x are solved by using the FE approach, and the

https://doi.org/10.1021/acsomega.2c06716
ACS Omega 2022, 7, 48447−48466

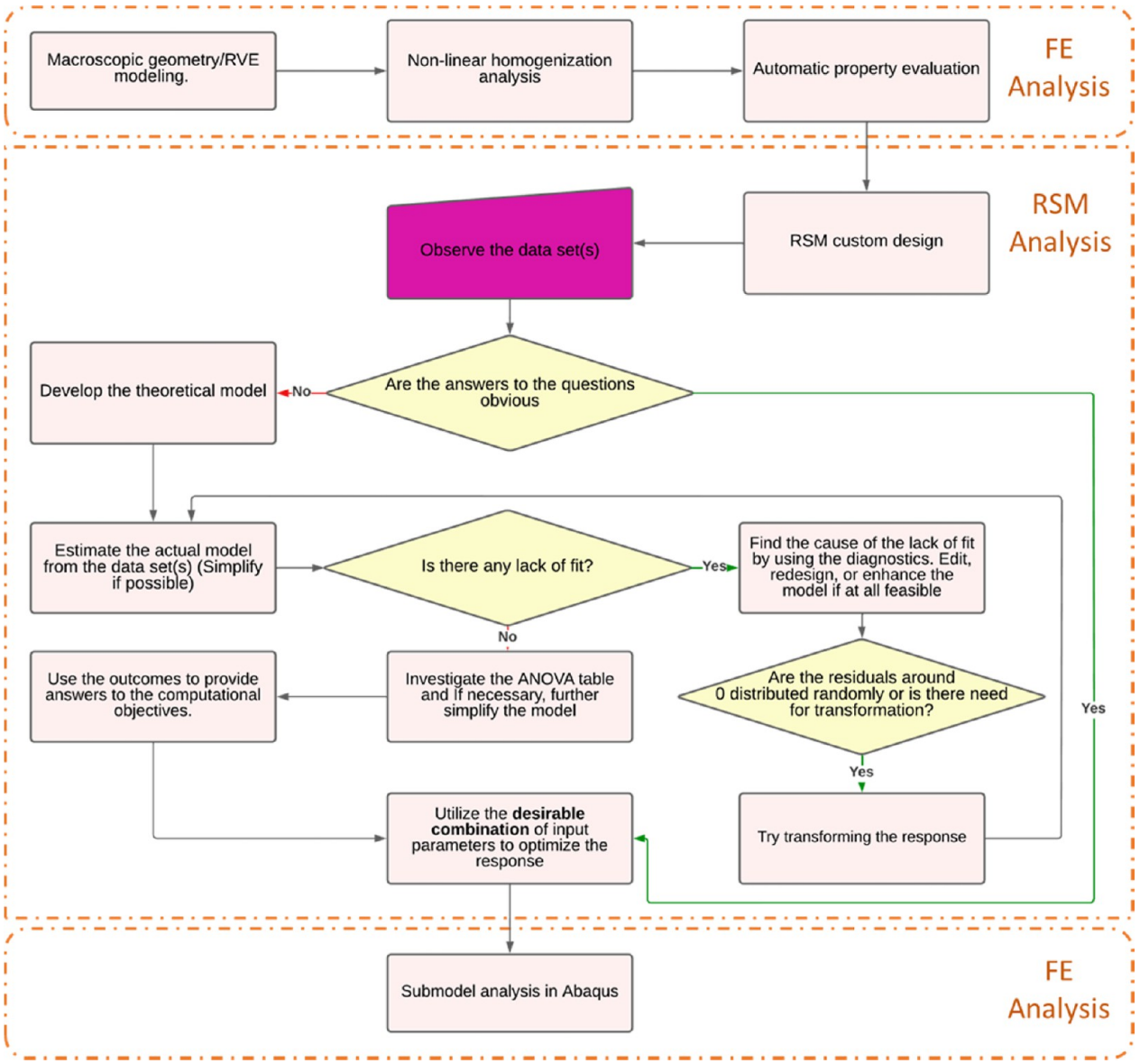

Figure 1. FE homogenization−RSM analysis steps.

effective heat flux vector $(\boldsymbol{q}) = (\boldsymbol{q})_1, (\boldsymbol{q})_2, (\boldsymbol{q})_3{}^{\mathrm{T}}$ may be produced by post-processing the results of the FE analysis and is presented as follows

$$\langle \boldsymbol{q} \rangle_i = \frac{1}{V_{\mathrm{RVE}}} \sum_{\mathrm{e}} V_{\mathrm{e}} \left(\sum_{l=1}^{\eta_{\mathrm{eint}}} \boldsymbol{q}_i(\boldsymbol{y}_l) \cdot \boldsymbol{W}(\boldsymbol{y}_l) \right) \text{ with } i = 1,2, \text{ and } 3 \tag{10}$$

where η_{eint} and η_{int} are the corresponding integers for the integration points in the element e and the whole RVE, respectively. The integration point weight $W(y)_i$ is located at an integration point at y_i in element e, whose volume is V_{e}. The effective heat flow vector $(\boldsymbol{q})_{\mathrm{i}}$ and the temperature gradient vector $\nabla \boldsymbol{T}_{\mathrm{j}}$ are then used to produce the effective thermal conductivity tensor $(\boldsymbol{k})_{\mathrm{ij}}$.

$$(\boldsymbol{k})_{\mathrm{ij}} = -\frac{(\boldsymbol{q})_{\mathrm{i}}}{\nabla \boldsymbol{T}_{\mathrm{j}}} \tag{11}$$

where the enforced temperature boundary condition $\nabla \boldsymbol{T}_{\mathrm{j}}$ allows for the calculation of the temperature gradient vector

$$\nabla \boldsymbol{T}_{\mathrm{j}} = \frac{\overline{\boldsymbol{T}}}{\boldsymbol{L}_{\mathrm{j}}} \tag{12}$$

where $\overline{\boldsymbol{T}}$ and L_j, respectively, stand for the enforced temperature boundary condition and the side length of the RVE ω in the direction of x_j.[27,37]

3. RESPONSE SURFACE METHODOLOGY

The response surface methodology (RSM) is a suggested way to lower computing costs. Response surfaces—also referred to as metamodels, surrogates, emulators, or auxiliary models—are streamlined versions of actual models. They approach the suggested input−output function of the underlying simulation model.[48] When dealing with issues where a small number of unrelated input factors significantly affect the response of interest (performance measure), the RSM is a combination of mathematical and statistical approaches that might be helpful.

https://doi.org/10.1021/acsomega.2c06716
ACS Omega 2022, 7, 48447−48466

Such methods can aid the development, enhancement, and optimization of processes.[49] Since the actual response function is unknown in most RSM cases, it is crucial to accurately approximate the response function and regulate specific parameters describing its quality. Since the RSM delivers practically immediate output parameters through approximate evaluation, it is frequently used to reduce the computing effort. Only a few design points can yield a high precision for the response function. Numerous metrics are used to regulate the response surface's quality. According to the standard method, the response function (functions) computation begins with a limited number of points, and the accuracy of the resulting approximation is checked at a few chosen verification points. If the quality is inadequate, refinement points are added to change the response surface.[32] The Design Expert program offers three alternative RSM designs: central composite, Box−Behnken, and optimal designs. The optimal (custom) design is used in this study. The run parameters for design are selected algorithmically to produce improved and optimized material for energy storage while limiting the number of runs as much as feasible. There are costs associated with this flexibility. Even if reconstructed with the same characteristics, a different design will probably be created. After creating the custom design, all pertinent factors for the FE and RSM analysis (Figure 1) were input into the models based on the data reported in Table 1 for this study with the preprocessing, FE analysis, and post-processing steps carried out in Digimat and ABAQUS software.

Table 1. Material Properties of the PEDOT:PSS (Matrix) and BNP (Inclusions)

properties	PEDOT:PSS	BNP
density (g/cm^3)	1.01−1.72[30,41,42]	2.53,[30] 2.49 (in this work)
Young's modulus (GPa)	0.5−2.7[30]	X = 1372.40, Y = 586.20[30]
shear modulus (GPa)		287.35[30]
specific heat capacity (J/g K)	2.37[42]	1.02[21]
thermal conductivity (W/m K)	$\Lambda_{\parallel} \approx 1.0$ and $\Lambda_{\perp} \approx 0.3$[43]	92.0 and 86.3[26]
electrical conductivity (S/cm)	752[18]	1.4×10^{-7}[18]
Poisson ratio	0.33[30,44]	$X = -0.04, Y = -0.02$ [25,26]
particle size (nm)	30[30,44]	30[19]
thickness (nm)		0.27−0.31,[19] 1.8, 4.7[40]
AR		0.04−0.1[30]
volume fraction		1−25% (in this work)

3.1. Analysis of Variance (ANOVA). ANOVA comprises computations that serve as a foundation for tests of significance and reveal the amounts of variability within a regression-related model. The models' veracity and predictive power are crucial factors in predictive modeling. The ANOVA is critical for determining the validity of the model, together with factorial designs and the resulting prediction equations.[50] The fundamental regression line concept is written as

$$(y_i - \bar{y}) = (\hat{y}_i - \bar{y}) + (y_i + \hat{y}_i) \tag{13}$$

where the first term, the second term, and the third term, respectively, represent the total variance in the response (y), the mean response variation, and the residual value. The result of squaring each of these terms and calculating the sum of all n observations is as follows

$$\sum (y_i - \bar{y})^2 = \sum (\hat{y}_i - \bar{y})^2 + \sum (y_i + \hat{y}_i)^2 \tag{14}$$

The square of the sample correlation (R^2) is calculated as the ratio of the model sum of squares to the total sum of squares as follows

$$R^2 = \frac{\sum (\hat{y}_i - \bar{y})^2}{\sum (y_i - \bar{y})^2} \tag{15}$$

The percentage of data variability that the regression model can account for is explained by eq 16. The sample correlation (R^2) scales from 0 to 1, with 1 denoting the ideal correlation. The sample variance (S_y^2) is defined as the ratio of the total sum of squares to the total degrees of freedom.

$$S_y^2 = \frac{\sum (y_i - \bar{y})^2}{n - 1} \tag{16}$$

Since there is just one independent variable in a simple linear regression model, the following is the mean square model (MSM)

$$\mathrm{MSM_{SLR}} = \frac{\sum (\hat{y}_i - \bar{y})^2}{1} \tag{17}$$

The mean square of a simple linear regression model is $\mathrm{MSM_{SLR}}$, as opposed to the comparable mean square error ($\mathrm{MSE_{SLR}}$), which is provided by

$$\mathrm{MSE_{SLR}} = \frac{\sum (y_i + \hat{y}_i)^2}{n - 2} \tag{18}$$

4. RESULTS AND DISCUSSION

4.1. Response Surface Methodology. *4.1.1. Model Development and Confirmation.* The use of the RSM in this work serves a dual purpose. The first reason is to create models for accurately predicting the mechanical and transport properties of PEDOT:PSS/BNP nanocomposite (such as effective elastic modulus, electrical conductivity, and thermal conductivity), and the second goal is to forecast the ideal factor combinations for the best electrode performance with the greatest level of desirability. The parameters for the selected factors and responses for the response surface design of the experiment are presented in Tables S1 and S2. As such, two blocks of data with 38 random treatments were needed for the optimal custom response surface approach of the FE design. Table S3 lists the combinations of each component level and the matching outcomes of response studies. The frequency distribution of the FE data for elastic modulus and electrical and thermal conductivities responses of the PEDOT:PSS/BNP nanocomposite electrode are shown in Figure S1. The models developed in this work were further validated with an additional four confirmation runs, as shown in Table S3. The result of the confirmation runs is presented in Table S4, which shows that the mean of the confirmation result falls within 95% of the upper and lower prediction intervals. This means that the models are adequate for accurately predicting the effective elastic modulus and electrical and thermal conductivities.

4.1.2. RSM Analysis of the Effective Elastic Modulus of the PEDOT:PSS/BNP Nanocomposite. We established and implemented a cubic functional model by statistically fitting the

https://doi.org/10.1021/acsomega.2c06716
ACS Omega 2022, 7, 48447−48466

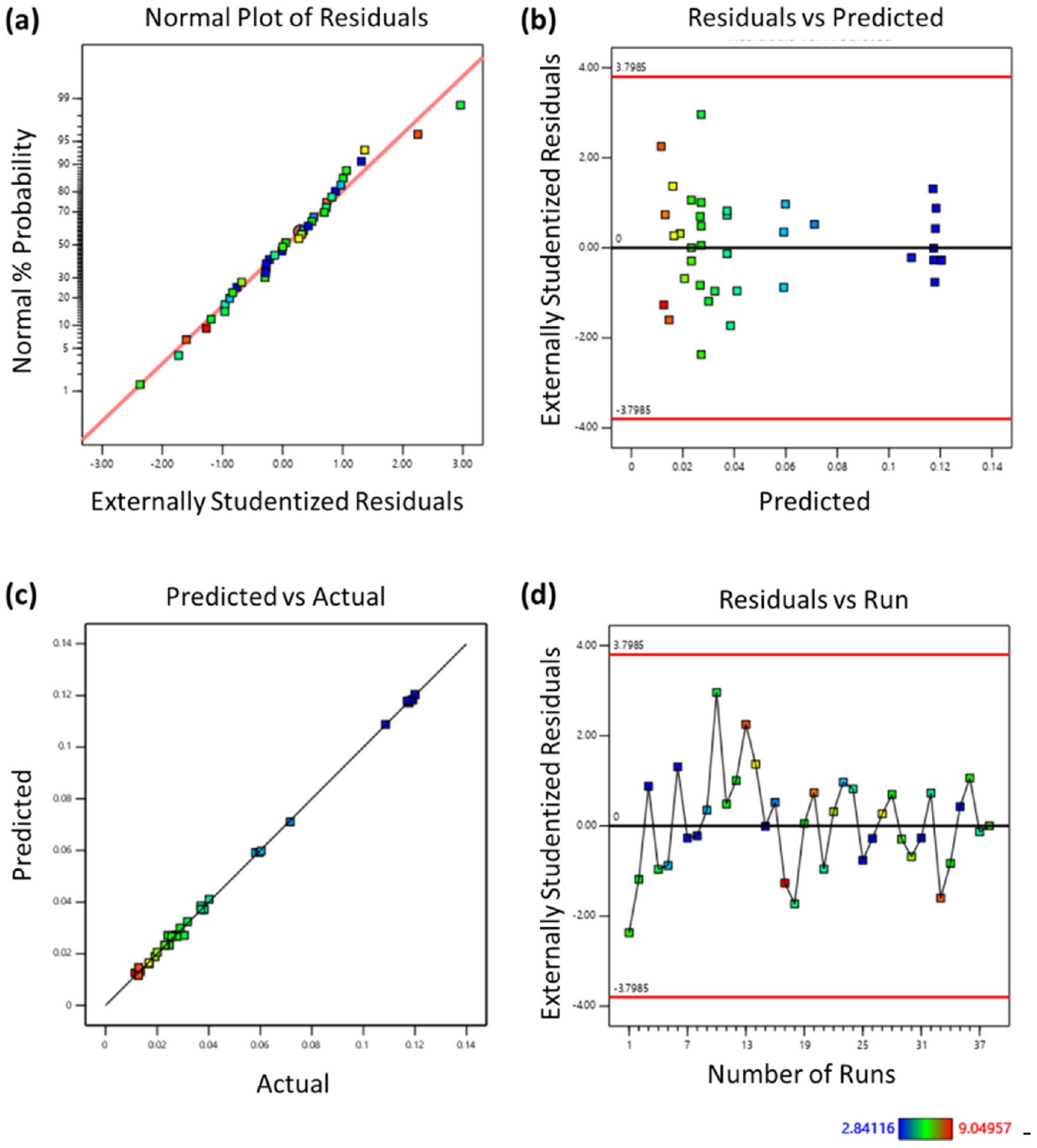

Figure 2. Diagnostic plots: (a) normal plot of residual, (b) residual vs predicted, (c) predicted vs actual, and (d) residual vs runs plots for the elastic modulus response of the PEDOT:PSS/BNP nanocomposite electrode.

isolated and interaction impacts of the parameters (factors) such as the volume content, AR, and orientation on elastic modulus (response), concluding that no other higher-order model was suitable. The statistical benchmarks for assessing the importance of the regression model include the regular coefficient of determination (R^2), adjusted coefficient of determination (Adj. R^2), predictive coefficient of determination (Pred. R^2), and sufficient precision values. The model's accuracy was demonstrated by the higher R^2 value of 0.9992.[34] The correlation between the predicted and measured values or the Adj. R^2 is used to represent how well the regression model fits the data. The FE results were quite compatible with the projected results because there was never much of a discrepancy between the adjusted R^2 (0.9986) and the predicted R^2 (0.9948). The ratio of the expected value range to the average prediction error is known as adequate precision (101.0219). The fact that the ratio was more than 4 demonstrated that the model was adequate for navigating the design space.[51,52]

https://doi.org/10.1021/acsomega.2c06716
ACS Omega 2022, 7, 48447−48466

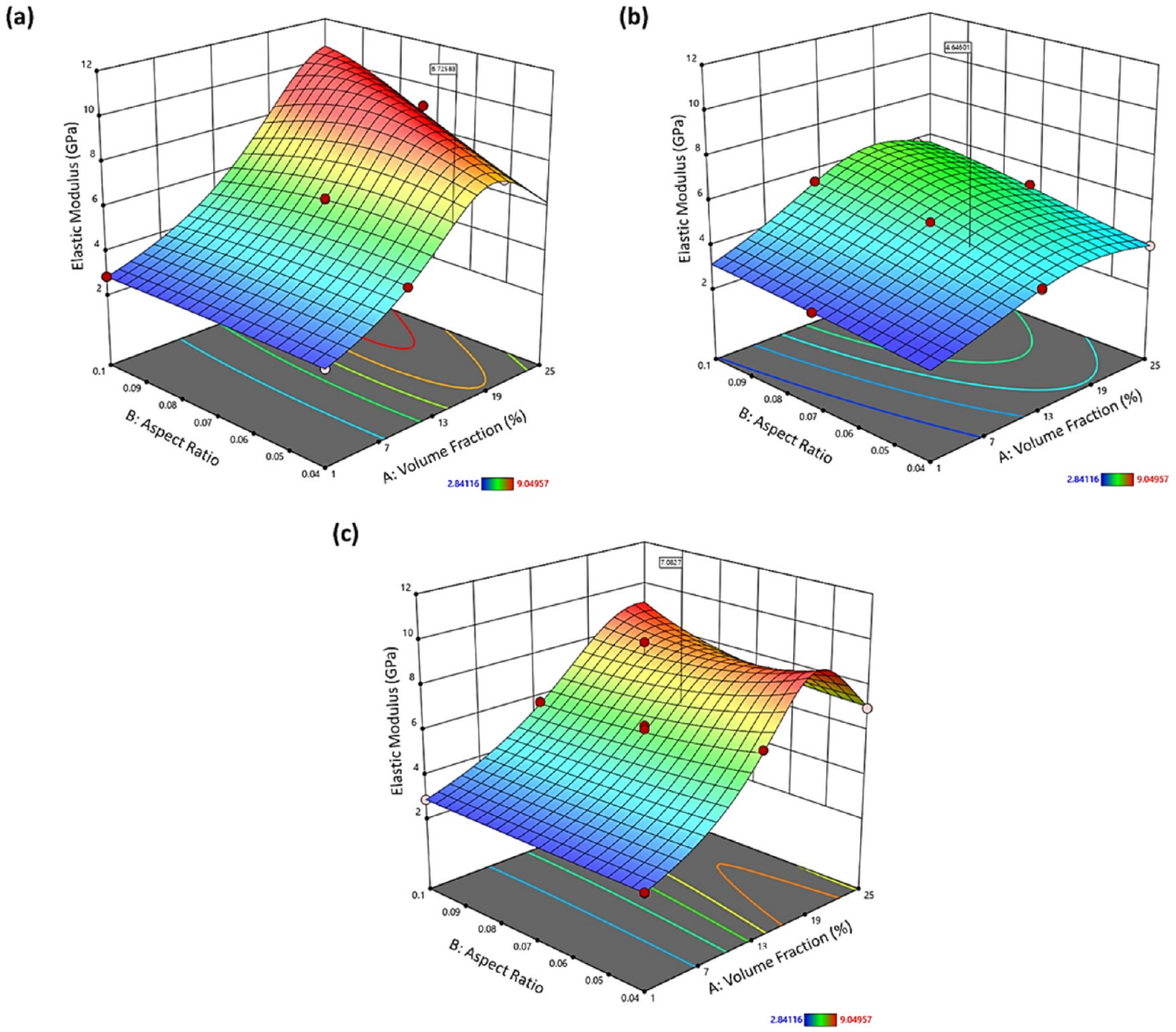

Figure 3. 3D contour plot of the effects of the volume fraction and AR at various orientations (a) 45°, (b) random, and (c) 90° on the elastic modulus response of the PEDOT:PSS/BNP nanocomposite electrode.

Besides, the plotted residual points nearly followed a straight line, as shown in Figure 2a, demonstrating that the residuals from the nonlinear model for elastic modulus were normally distributed and that there was no association between the errors at any given position. The residuals are shown against growing expected response values in Figure 2b. The distribution of residuals at random inside the graph's red boundaries indicates high model prediction.[53] The effective elastic modulus values found by the FE analysis were in agreement with the curve fit to the prediction function, as shown in Figure 2c. The residual run order plots in Figure 2d depict the pattern of data composition by plotting each residual in relation to an index. According to the sinusoidal distribution of data points along the run order, there is no discernible model drift inside the composite's elastic behavior. In other words, there is no discernible rise or fall in the model's anticipated variables.[54] The created elastic modulus model is adequate and adaptable to predict the impacts of the volume fraction, AR, and orientation, according to these diagnostic charts.

The findings of the cubic elastic modulus model's ANOVA analysis are shown in Table S5. Since the cubic model's p-value was substantially lower than 0.05, it was clear that the model successfully captured a statistically significant correlation. The model provided a good approximation because the p-value of the lack of fit term was more than 0.1, which is not significant. A, B, C, AB, AC, BC, A^2, B^2, ABC, A^2B, B^2C, and A^3 all had p-values under 0.05 among the isolated and interaction components, showing a statistically significant impact on the effective elastic modulus value predicted by the cubic model. We applied power transformation and eliminated the insignificant cubic terms. This led to the development of a functional connection between elastic modulus and the variables, as presented in eq 19.

https://doi.org/10.1021/acsomega.2c06716
ACS Omega 2022, 7, 48447−48466

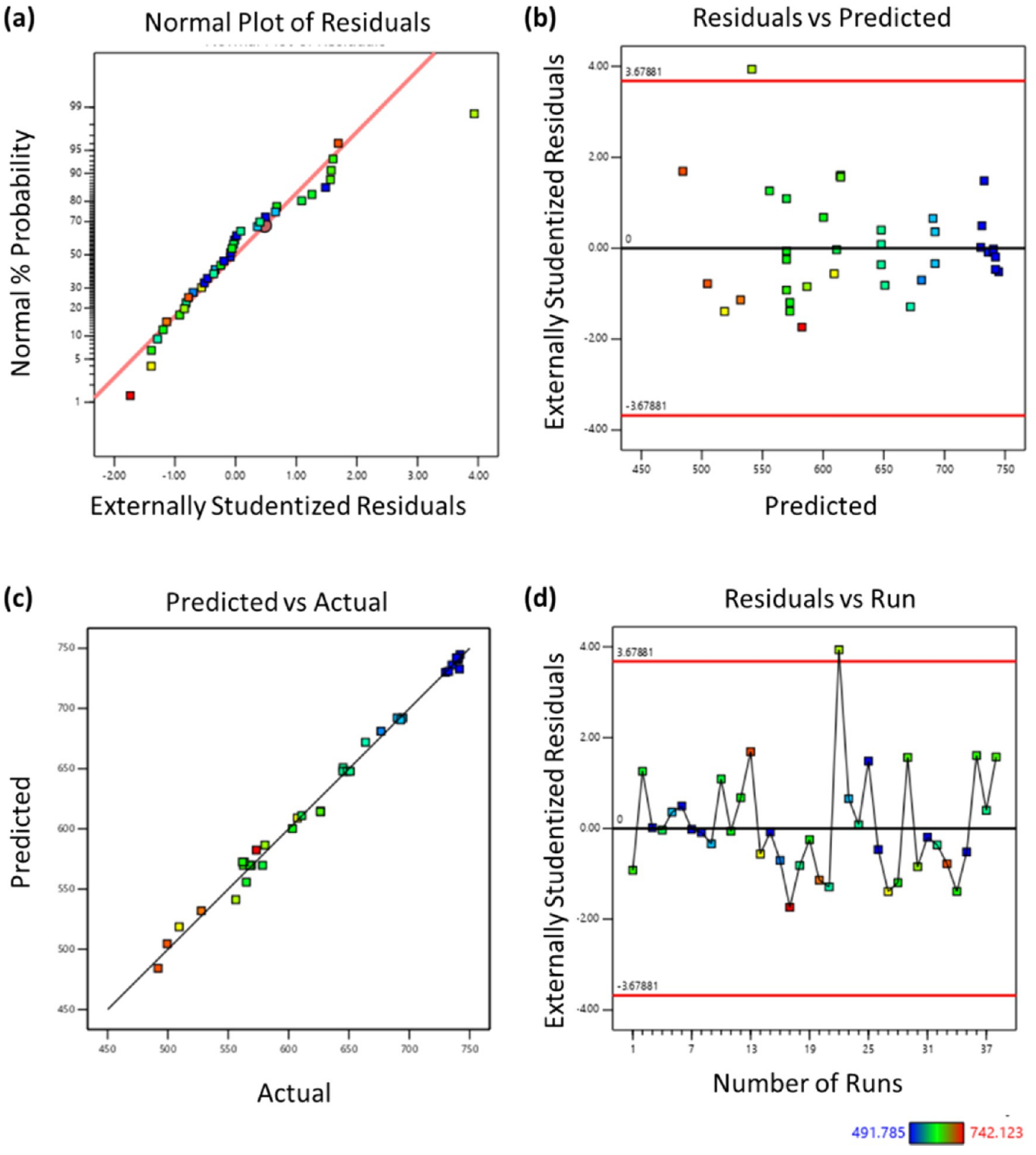

Figure 4. Diagnostic plots: (a) normal plot of residual, (b) residual vs predicted, (c) predicted vs actual, and (d) residual vs runs plots for the electrical conductivity of the PEDOT:PSS/BNP nanocomposite electrode.

https://doi.org/10.1021/acsomega.2c06716
ACS Omega 2022, 7, 48447−48466

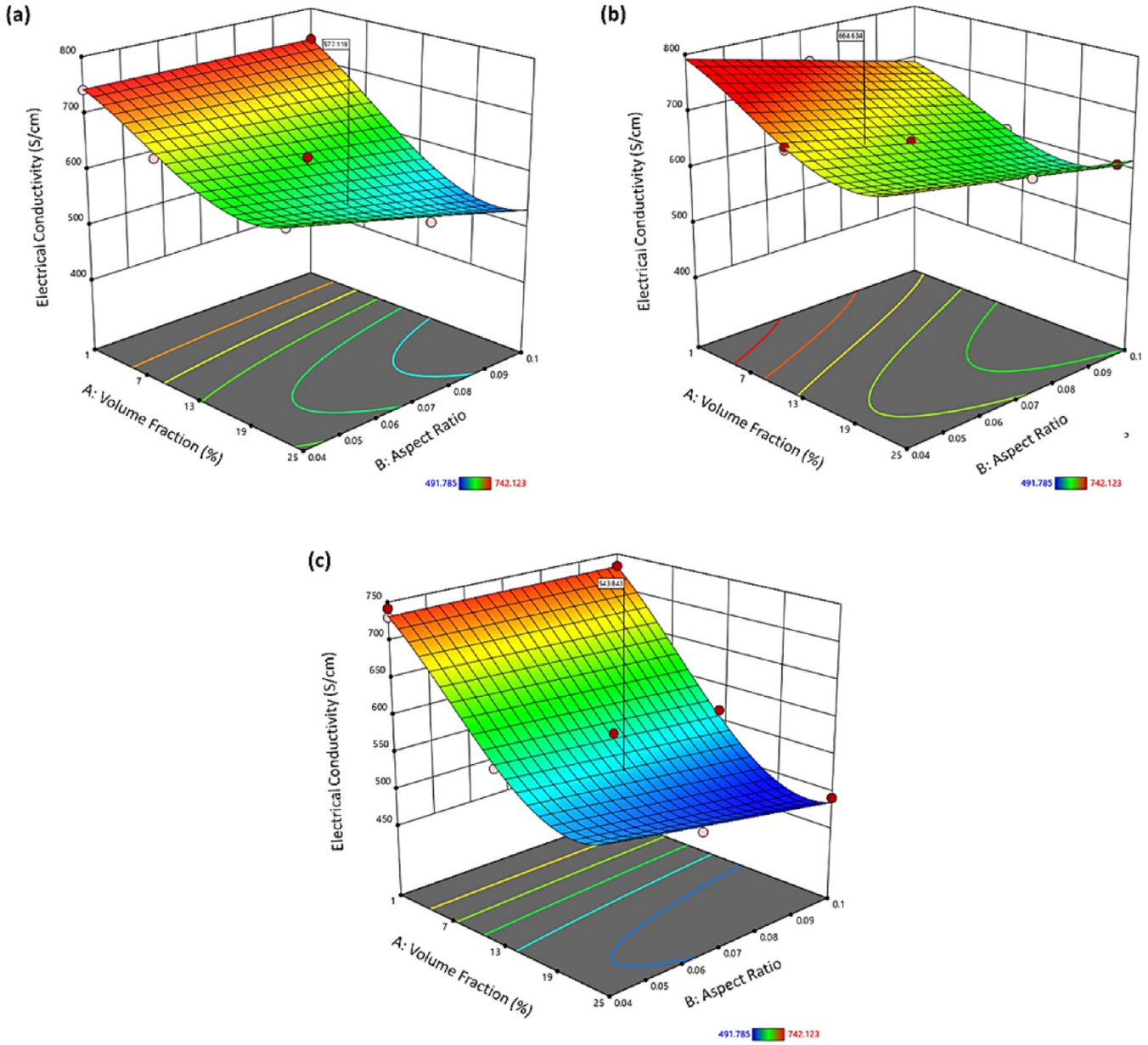

Figure 5. 3D contour plot of the effects of the volume fraction and AR at various orientations (a) 45°, (b) random, and (c) 90° on the electrical conductivity response of the PEDOT:PSS/BNP nanocomposite electrode.

$$
\begin{aligned}
&(\textit{Elastic modulus})^{-2.03} \\
&\quad = +0.0293 - 0.0401A - 0.0021B + 0.0017C[1] \\
&\qquad - 0.0040C[2] - 0.0003AB + 0.0001AC[1] \\
&\qquad - 0.0040AC[2] + 0.0007BC[1] + 0.0059BC[2] \\
&\qquad + 0.0410A^2 + 0.0025B^2 + 0.0015ABC[1] \\
&\qquad - 0.0027ABC[2] - 0.0066A^2B - 0.0025B^2C[1] \\
&\qquad - 0.0016B^2C[2] - 0.0073A^3 \qquad (19)
\end{aligned}
$$

Figure 3 shows the 3D contour plot of the effects of the volume fraction and AR at various orientations (45°, random, and 90°) on the elastic modulus response of the BNP/PP nanocomposite electrode. It can be observed that the impact of the AR on the elastic modulus of the nanocomposite at the low volume content of BNPs is negligible for all orientations. However, when the inclusions are tilted at 45° (Figure 3a), the modulus increases as the volume fraction increases. This increment is more noticeable when the AR is low. Meanwhile, for a high AR, the elastic modulus increases with the increase in volume fraction from 1% to about 19% and then decreases as the volume fraction continues to increase from 19 to 25%. The maximum elastic modulus response for the BNP inclusions inclined at 45° is obtained when the AR is 0.1 and the volume fraction is at 25%. Due to the evenly distributed stiffness in two dimensions by the anisotropic BNP, this relationship can be underpinned. When the BNP fillers are randomized (Figure 3b), the modulus increases slightly from 1% volume content to 19% and then decreases from there to 25%. However, this increase is more apparent for a low AR than for a high AR at an angle of 90° (Figure 3c), and the resistance to deformation upon stress application increases as the volume content of BNP increases for high AR values of up to 19% before declining. A similar trend is observed when the AR is low. However, when the AR is about

https://doi.org/10.1021/acsomega.2c06716
ACS Omega 2022, 7, 48447−48466

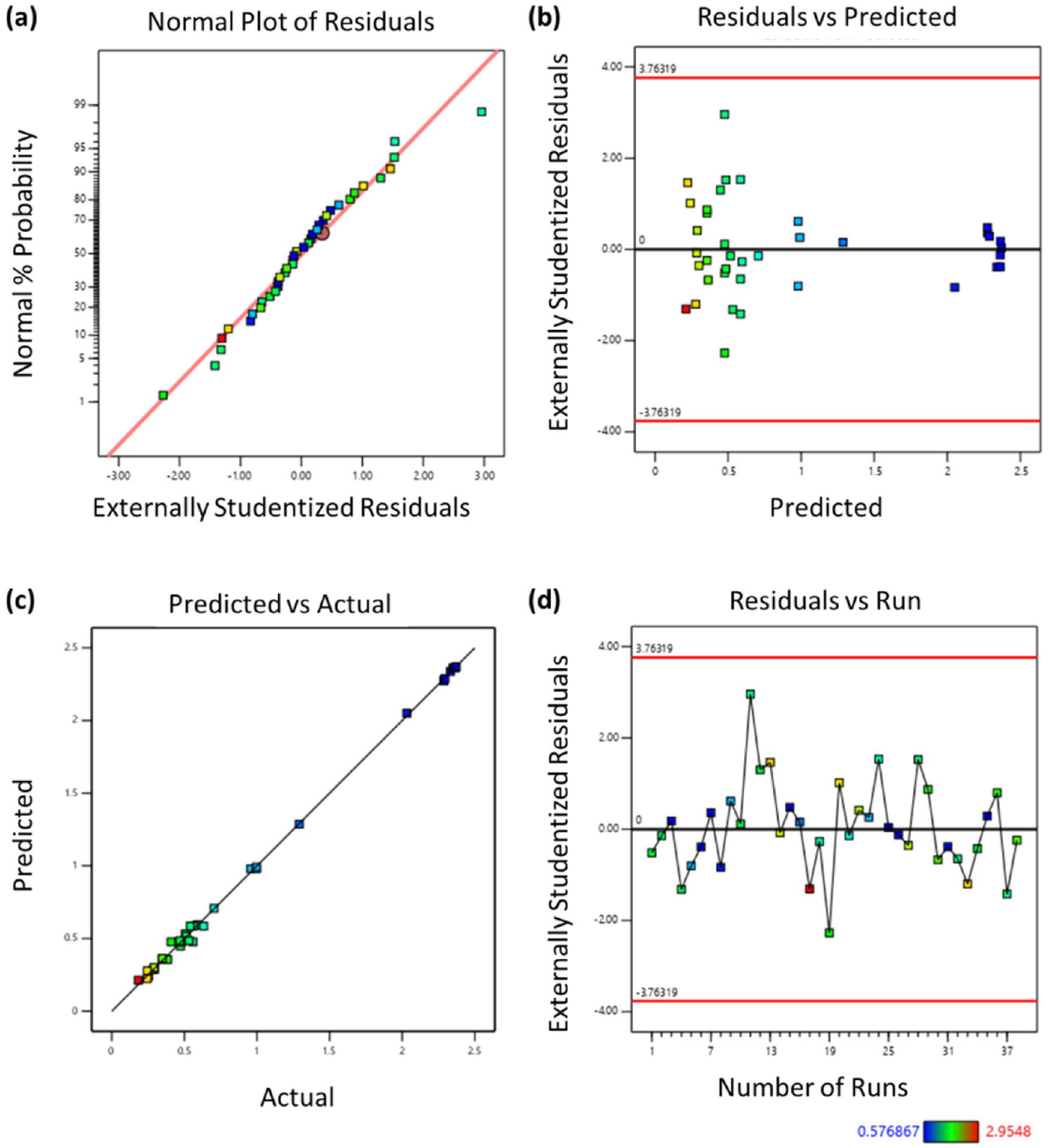

Figure 6. Diagnostic plots: (a) normal plot of residual, (b) residual vs predicted, (c) predicted vs actual, and (d) residual vs runs plots for the thermal conductivity response of the nanocomposite electrode.

0.07, the modulus was slightly lower at the peak of the volume content. In general, it is shown that across the average effect of various orientations (Figure S2), the elastic modulus increases with the BNP inclusion volume fraction.

4.1.3. RSM Analysis of the Effective Electrical Conductivity of the PEDOT:PSS/BNP Nanocomposite. Similar to the elastic modulus model, a cubic model, which is the highest-order irreplaceable model fittable, was developed and adopted to predict the impact of the volume fraction, AR, and orientation on the effective electric conductivity response of the PEDOT:PSS/BNP nanocomposite electrode. The model fits the data well enough to analyze and predict the effective electrical conductivity, as indicated by the R^2, adjusted R^2, predicted R^2, and adequate precision values of 0.9925, 0.9883, 0.9705, and 48.7543, respectively (Table S6). The adjusted R^2 value was less than 0.2 from the expected R^2 value, showing that the FE and RSM predicted values of the effective electrical conductivity of the nanocomposite were quite similar. The

https://doi.org/10.1021/acsomega.2c06716
ACS Omega 2022, 7, 48447−48466

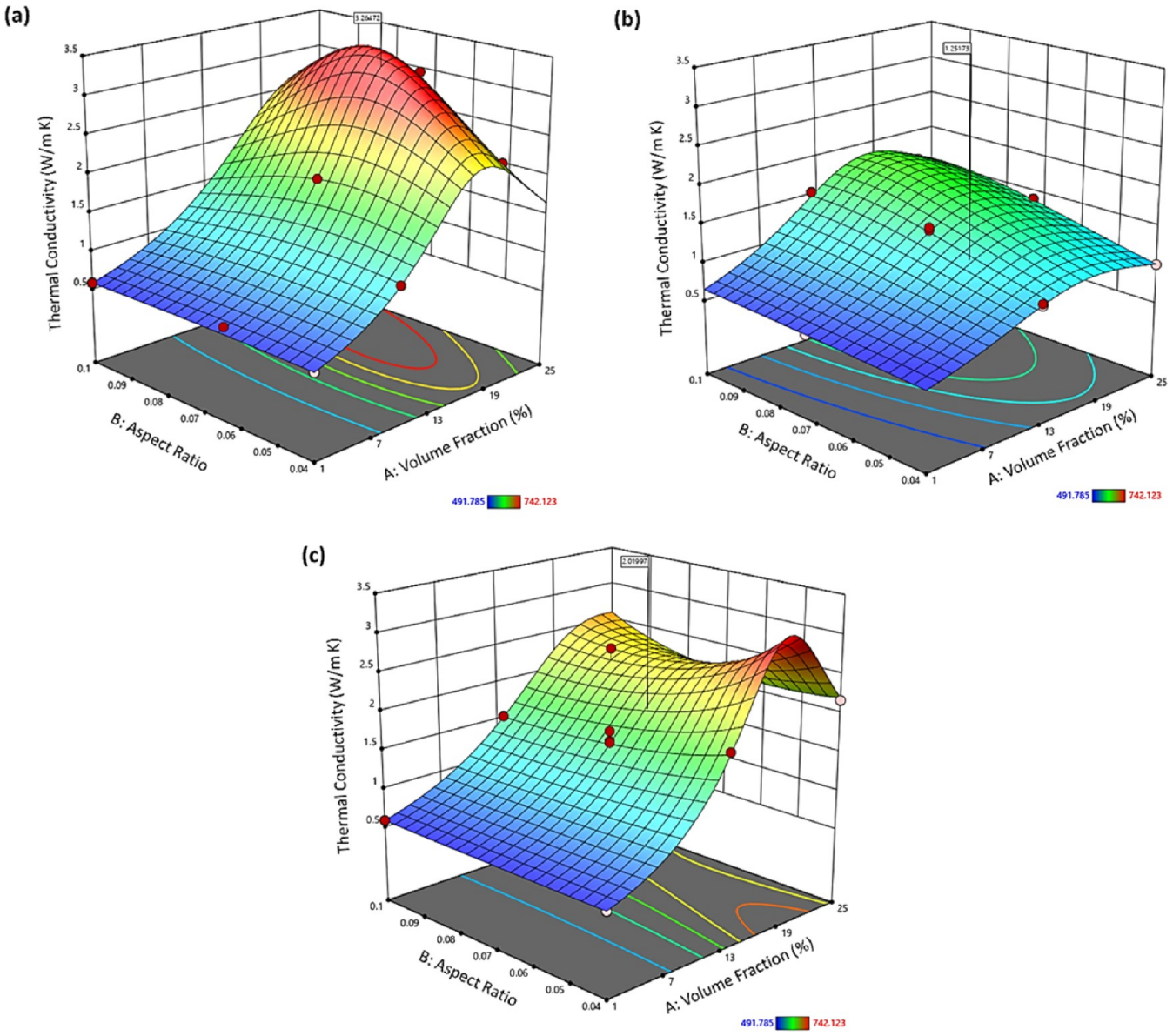

Figure 7. 3D contour plot of the effects of the volume fraction and AR at various orientations (a) 45°, (b) random, and (c) 90° on the thermal conductivity response of the PEDOT:PSS/BNP nanocomposite electrode.

significance of the lack of fit is shown by the lack of fit's F value of 8.35. The probability of noise causing a significant lack of fit is about 0.07%.

However, upon further investigation of the diagnostic plots, the plotted residual points almost followed a straight line, as shown in Figure 4a, demonstrating that the residuals from the nonlinear model for effective electrical conductivity response were normally distributed and that there was no association between the errors at different sites, except for the outlier observed for run 22. The high model prediction is shown by the random distribution of residuals inside the red bounds of the graph in Figure 4b, except for an outlier that corresponds to the electrical value obtained for run 22. Besides, it can be seen in Figure 4c that the effective electrical conductivity values determined by the FE analysis were consistent with the curve fit to the prediction function. The residual versus run plot in Figure 4d, which plots each residual with respect to an index (run), shows the pattern of data composition. The sinusoidal distribution of data points along the run order indicates that there is no appreciable model drift in predicting the effective electrical conductivity behavior of the composites. The *p*-values of *A*, *B*, *C*, *AB*, *AC*, *BC*, A^2, *ABC*, and A^3 among the main and interaction effects were all less than 0.05, showing their statistically significant influence on the value of electrical conductivity predicted by the cubic model. This led to the development of a functional relationship, shown in eq 20, between effective electrical conductivity and the different factors.

$$\begin{aligned}\text{Electrical conductivity} &= +610.22 - 119.16A - 28.09B - 20.92C[1] \\ &\quad - 18.11C[2] - 11.34AB - 15.84AC[1] \\ &\quad - 16.14AC[2] + 6.92BC[1] + 7.15BC[2] + 51.80A^2 \\ &\quad + 6.06ABC[1] - 9.16ABC[2] + 42.32A^3 \end{aligned} \quad (20)$$

The effects of the volume fraction and AR at different orientations (45°, random, and 90°) on the electrical

https://doi.org/10.1021/acsomega.2c06716
ACS Omega 2022, 7, 48447−48466

conductivity response of the BNP/PP nanocomposite electrode are shown in the 3D contour plots in Figure 5. The electrical conductivity of the nanocomposite depends significantly on the AR and volume fraction for different orientations. The electrical conductivity diminishes as the volume fraction increases when the inclusions are oriented at a 45° angle (Figure 5a). When the AR is low, this deterioration is more obvious. The electrical conductivity increases with the increase in the AR from 0.1 to about 0.04 at a high volume percent. The poor electrical conductivity of BNPs in comparison to that of PP is responsible for this decrement in electrical conductivity with increasing vol %. Similar trends may be seen when the BNP fillers are randomized (Figure 5b), although the decline is not as sharp as it is when the filler is tilted at a 45° angle. This behavior can be ascribed to the filler being evenly distributed throughout. At an angle of 90° (Figure 5c), this reduction in electrical conductivity of the nanocomposite follows a steep decline as the content of the BNP increases. In general, from the overall effect across all the different orientations, the electrical conductivity of the composite dwindles as the volume fraction of the BNP increases (Figure S3).

4.1.4. RSM Analysis of the Effective Thermal Conductivity of the PEDOT:PSS/BNP Nanocomposite. To predict the main and interaction effects of the volume fraction, AR, and orientation on the effective thermal conductivity response of the PEDOT:PSS/BNP nanocomposite electrode, the cubic terms added to the model developed improved the model and were used. The model fits the data well enough to analyze and estimate the effective thermal conductivity, with R^2 = 0.9989, adjusted R^2 = 0.9980, predicted R^2 = 0.9959, and adequate precision value = 86.0746 (Table S7). The adjusted R^2 value was less than 0.2 of the expected R^2 value, demonstrating that the effective thermal conductivity of the nanocomposite was predicted by both the FE and RSM to be relatively comparable. The model provided a good approximation because the lack of fit term's p-value was more than 0.1, which is not statistically significant.

$$\begin{aligned}(\textit{Thermal conductivity})^{-1.57} &= +0.4714 - 0.7307A - 0.0314B + 0.0642C[1] \\ &\quad - 0.0549C[2] - 0.0261AC[1] - 0.0607AC[2] \\ &\quad + 0.0099BC[1] + 0.1017BC[2] + 0.8671A^2 \\ &\quad + 0.0654B^2 + 0.0346ABC[1] - 0.0448ABC[2] \\ &\quad - 0.1027A^2B - 0.0735B^2C[1] - 0.0324B^2C[2] \\ &\quad - 0.2299A^3 \end{aligned} \tag{21}$$

The residuals from the nonlinear model for effective thermal conductivity response were normally distributed and essentially followed a straight line, as shown in Figure 6a, indicating that there was no correlation between the errors at various locations. The random distribution of residuals inside the red borders of the graph in Figure 6b illustrates the high model prediction. Furthermore, the effective thermal conductivity values calculated by the FE were in line with the curve fit to the prediction function, as shown in Figure 6c. The pattern of data composition may be seen in the residual against the run plot in Figure 6d, which plots each residual with an index (run). The sinusoidal distribution of data points along the run order suggests that the composites' actual thermal conductivity behavior is predicted by the model without experiencing a substantial model drift. The main and interaction effects' p-values for A, B, C, AC, BC, A^2, B^2, ABC, A^2B, and B^2C were all less than 0.05, indicating their statistical significance in influencing the effective thermal conductivity value predicted by the cubic model. As a result, a functional power transformed the relationship between effective thermal conductivity and the various factors for better prediction was created, as given in eq 21 (with $\lambda = -1.57$).

The effects of the volume fraction and AR at different orientations (45°, random, and 90°) on the thermal conductivity response of the PEDOT:PSS/BNP nanocomposite electrode are depicted in Figure 7 as 3D contour plots. It can be seen that for all orientations, the impacts of the AR and volume fraction on the thermal conductivity of the nanocomposite are considerable. As a result, the thermal conductivity increases as the volume percentage increases from 1 to 25% when the inclusions are oriented at 45° (Figure 7a). When the AR is 0.07, the increase is more apparent. This location marks the electrode's maximal response point. The thermal conductivity of the nanocomposite improves slightly from 1 to 19% and then declines from there to 25% when the BNP fillers are randomized (Figure 7b). However, this increase is more noticeable for a low AR than for a high AR. The thermal conductivity increases substantially as the volume content of the BNP increases for both high and low AR values up to around 19% before receding (Figure 7c) at an angle of 90°. Comparing the AR at a 19% volume fraction, the thermal conductivity is slightly lower for the 90° than for the 45° at 0.07. The thermal conductivity of the electrode increases with the increasing volume fraction up to 19% before declining across the average effect of the different orientations (Figure S4).

4.1.5. Optimization/Desirability. The desirability function analysis, is a widely used technique in the sector for streamlining numerous response procedures. It is predicated on the notion that a product or process's "quality" is wholly unsatisfactory if it possesses many quality attributes, one of which is outside of certain desirable boundaries. The approach looks for x operational parameters that provide the "best desired" response values. In particular, each response's estimated value is converted to individual desirability between 0 and 1 or scale-free desirability. A value of 1 is entirely desirable, whereas a value of 0 is entirely undesirable. The geometric mean is then used to add together all the desirability values, resulting in the overall desirability D, which is shown as follows[55,56] (eq 22).

$$D = \left[\prod_{j=1}^{N} d_i\right]^{1/\sum r_i} \tag{22}$$

where N represents the number of responses, d_i denotes the individual desirability of each response, and r_i is the weight of d_i.[55] Different functions $d_i(Y_i)$ can be used depending on whether a specific response Yi is to be maximized, reduced, or given a goal value. Derringer and Suich[57] suggested a practical class of desire functions. Let L_i, U_i, and T_i represent the response Y_i's intended lower, higher, and goal values, respectively, with $L_i \leq T_i \leq U_i$. The individual desirability is defined as follows if a response is to be maximized instead

$$d_i(\hat{Y}_i) = \begin{cases} 0 & \text{if } \hat{Y}_i(x) < L_i, \\ \left(\dfrac{\hat{Y}_i(x) - L_i}{T_i - L_i}\right)^s & \text{if } L_i \leq \hat{Y}_i(x) \leq T_i, \\ 1 & \text{if } \hat{Y}(x) > T_i \end{cases} \tag{23}$$

https://doi.org/10.1021/acsomega.2c06716
ACS Omega 2022, 7, 48447−48466

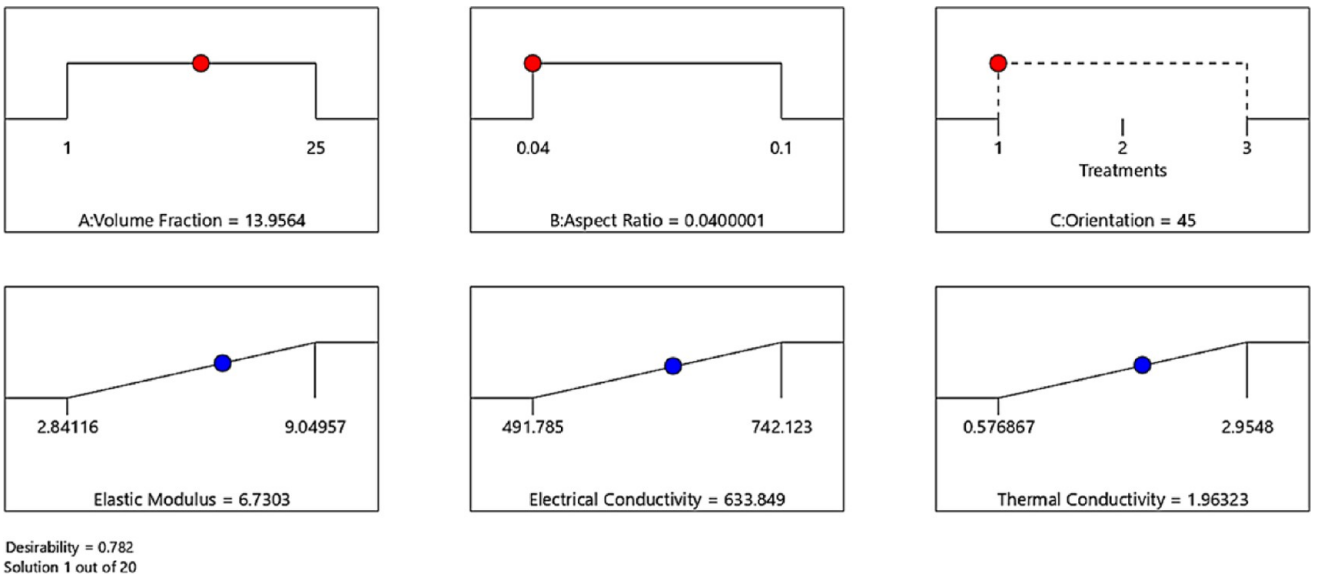

Figure 8. Ramp function graph showing the optimized response values based on the overall desirability of the factor combination.

with T_i being considered in this instance as a significant number for the response.[56,58]

The responses were all assigned equal weight and importance; this is because they are all important characteristic parameters for the effective performance of an electrode. The optimum solution with a desirability of 0.78 was generated using the models developed for estimating the transport characteristics and mechanical integrity of the electrode. The optimized solution had the following factor combinations: volume fraction = 13.96%, AR = 0.04, and orientation = 45°. These factors translate to optimized responses of effective elastic modulus = 6.73 GPa, effective electrical conductivity = 633.85 S/cm, and effective thermal conductivity = 1.96 W/m K (Figure 8). The overall desirability for the response across orientations of the inclusion is shown in Figure 9. Figure 9a displays the 3D desirability plot for the elastic modulus (max), electrical conductivity (max.), and thermal conductivity (max.) responses of the BNP/PP nanocomposite electrode at 45° inclination of the BNP inclusions. The 3D desirability plot for responses of an electrode with randomized BNP inclusions is shown in Figure 9b. Similarly, the 3D desirability plot for the responses of the nanocomposite at a 90° angle is shown in Figure 9c. It can be seen that the volume fraction of the BNP inclusions contribute significantly to the overall desirability of the responses. The desirability for maximizing the responses increases as the volume content of the BNP increases for all orientations. The periodic RVEs for the optimized PP matrix, the BNP inclusions inclined at 45°, and their nanocomposite are presented in Figure 10.

4.2. FE Analysis for Optimized Responses. The RSM was used to optimize the response variables of the transport characteristics of the nanocomposite based on the findings of the FE simulation. Thereafter, the effective elastic modulus, electrical conductivity, and thermal conductivity of optimized nanocomposites were further examined for an in-depth FE study in the following section.

4.2.1. FE Analysis for the Elastic Modulus of the PEDOT:PSS/BNP Nanocomposite. The elastic modulus, poison ratio, and shear modulus of the improved composites were all evaluated using FE analysis and the aforementioned material properties. With an axial elastic modulus of 4.71 GPa and an in-plane elastic modulus of 10.36 GPa, the composite has an average effective elastic modulus of 6.57 GPa. Besides, with a 3% error margin, the effective elastic modulus predicted by the RSM is close to this result (Table 2). The values of transverse Poisson's ratio, ν_{12}, of 0.13, in-plane shear modulus, G_{12}, of 2.33 GPa, transverse shear moduli, G_{13} and G_{23}, of 2.38 GPa and 2.32 GPa, respectively, were all displayed by the electrode. This result suggests that the nanocomposite can withstand stresses associated with the metal ion intercalation during charging and discharge cycles. The linear stress−strain curve of the optimized PEDOT:PSS/BNP nanocomposite shows that the electrode is elastic up to 0.14% (Figure 11). This suggests that the electrode is mechanically stable for volume variations inside the electrode that originate from metal ion intercalation limited to 0.14%. Figure 12 displays the maximum principal strain, von Mises stress, and displacement distribution for the RVE of BNP inclusions, the PEDOT:PSS matrix, and the PEDOT:PSS/BNP nanocomposite under general 3D loading. It can be seen that PEDOT:PSS strains more than the BNP; meanwhile, the majority of the stress is carried by the BNP inclusion. In Figure S5, the displacement components U_1, U_2, and U_3 for the inclusion, matrix, and nanocomposite are shown.

4.2.2. FE Analysis for the Electric Conductivity of the PEDOT:PSS/BNP Nanocomposite. Similar to the mechanical properties, the effective electrical conductivity for the PEDOT:PSS/BNP nanocomposite with the BNP inclusion was calculated with volume fractions of the inclusion ranging from 1 to 25 vol % and the AR from 0.04 to 0.1. The optimized nanocomposite predicted by the FE analysis has an average effective electrical conductivity of 619 S/cm (Table 3). This result is comparable to the conductivity predicted by the RSM, which has an error margin of 3%. The nanocomposite can be compared to conductive metallic electrodes due to the magnitude of its electron transport. Despite this, it is clear that this value is lower than the PP's electrical conductivity, which is 752 S/cm. Considering that the BNP has a poor electrical conductivity (1.4×10^{-7} S/cm), this drop in conductivity is attributable to it. Figure 13 shows the highest values of the electrical current density, ECD, and EPOT, for the RVE of the BNP inclusions, PEDOT:PSS matrix, and their nanocomposite under uniaxial macroscopic voltage gradient loading in the 1-, 2-, and 3-directions. The highest current flow across the nano-

https://doi.org/10.1021/acsomega.2c06716
ACS Omega 2022, 7, 48447−48466

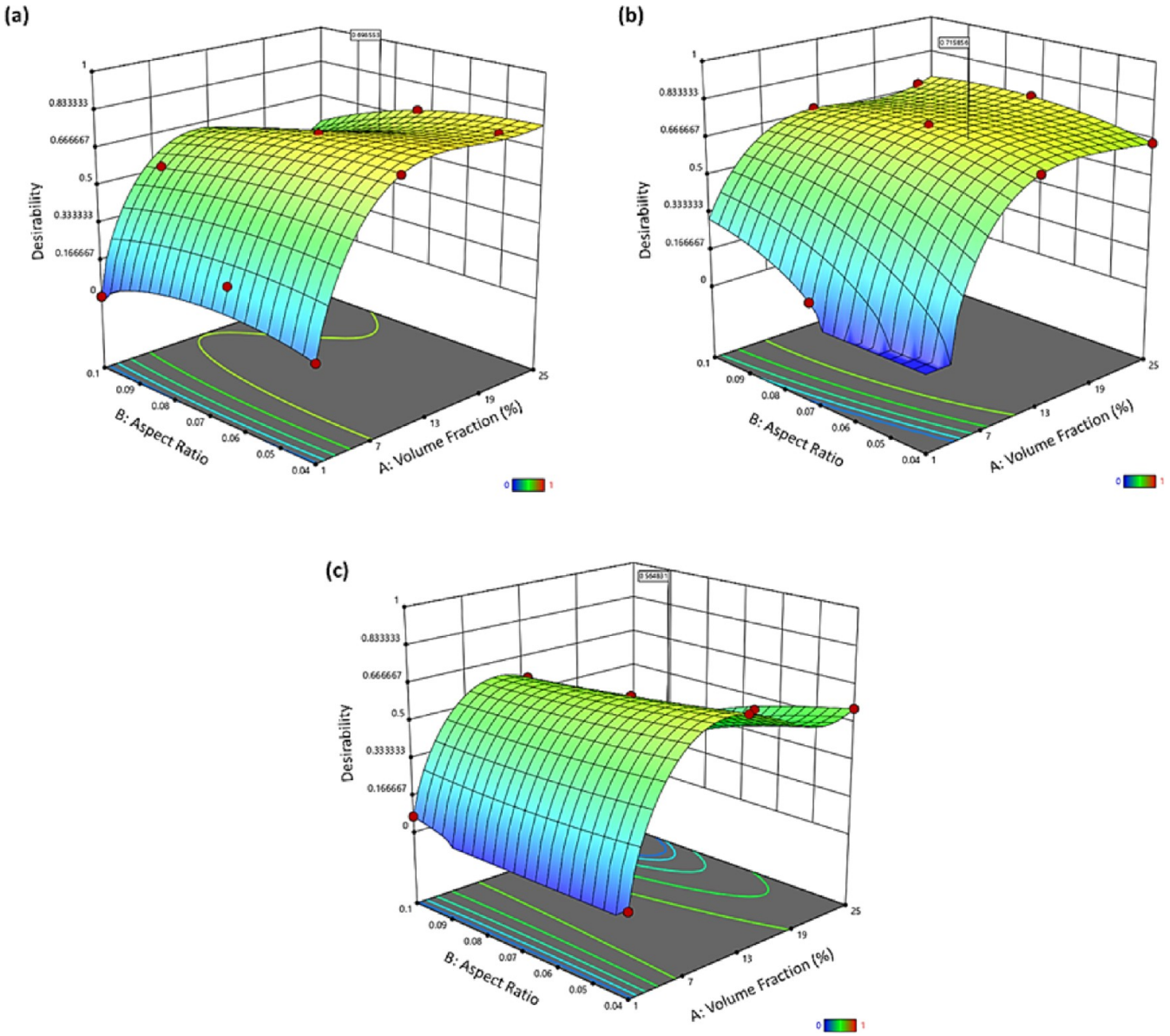

Figure 9. 3D contour plot of the desirability of the volume fraction and AR at various orientations (a) 45°, (b) random, and (c) 90° based on the optimized elastic modulus (max) and electrical conductivity (max.) and thermal conductivity (max.) responses of the PEDOT:PSS/BNP nanocomposite electrode.

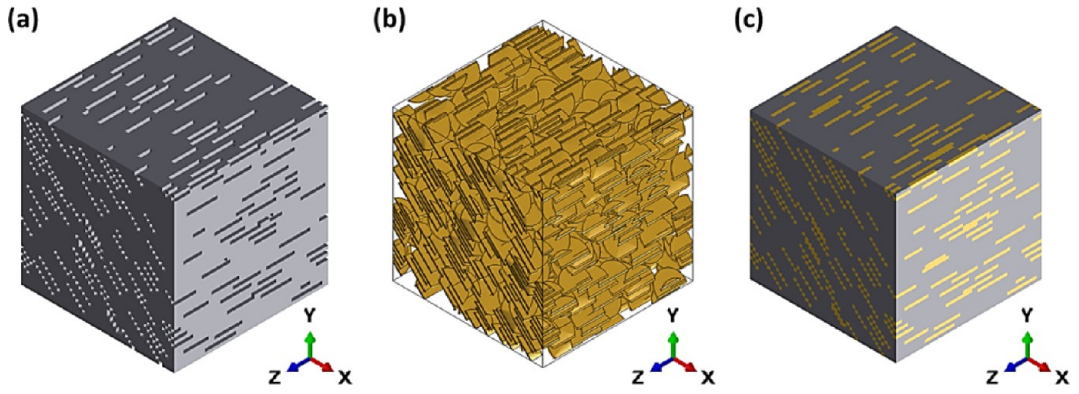

Figure 10. Periodic RVEs for (a) matrix, (b) BNP inclusions inclined at 45°, and (c) mesh of their nanocomposite.

composite is mostly accounted for by the electron transport of the conjugated system of the PEDOT:PSS backbone chain, as seen by the ECD distribution in the nanocomposite flowing through the interface of the BNP and PEDOT:PSS. Since the

https://doi.org/10.1021/acsomega.2c06716
ACS Omega 2022, 7, 48447−48466

Table 2. FE Homogenization Technique and RSM Prediction of the Effective Modulus of the Optimal PEDOT:PSS/BNP Nanocomposite

	effective modulus					
	FE (GPa)					
s/n	E_1	E_2	E_3	average	RSM (GPa)	error (%)
1	4.71	10.36	4.65	6.57	6.73	2.43

greatest electrical potentials at each node in the nanocomposite are almost equal in magnitude, the EPOT, it indicates that the BNP is evenly distributed. For the inclusion, matrix, and nanocomposite along the 1-, 2-, and 3-directions, Figures S6–S8 depict the distribution of the magnitude of ECD, electric potential gradient, and EPOT. Additionally, Figures S9–S11 show the ECD components ECD_1, ECD_2, and ECD_3 for the inclusion, matrix, and nanocomposite along directions 1, 2, and 3.

4.2.3. FE Analysis for the Thermal Conductivity of the PEDOT:PSS/BNP Nanocomposite. The FE analysis is used to evaluate the optimized PEDOT:PSS/BNP nanocomposite's heat transport capability, that is, its phonon movement. In comparison to the thermal conductivity predicted by the RSM, the average effective thermal conductivity is 1.97 W/m K, which is around a 0.6% error difference. Table 4 shows the effective thermal conductivities of the optimal PEDOT:PSS/BNP nanocomposite as predicted by the FE analysis and RSM. From the FE result, the axial thermal conductivity is 1.91 W/m K, whereas the in-plane thermal conductivity is 2.73 W/m K. Since the direction of the inclusion is responsible for much of the phonon transport, as indicated by the maximum heat flow, this anisotropic behavior may be explained. Furthermore, because phonon and electron movements determine the thermal conductivity in any material, the value of thermal conductivity is separated into two main parts: $k = k_e + k_p$, where k_e is the thermal conductivity caused by electron movement and k_p is the thermal conductivity induced by phonons transport. According to the Wiedermann–Franz law (eq 24), the poor electrical conductivity of the BNP causes a low thermal conductivity generated by electron movement. As a result, as illustrated in Figure 14, the temperature gradient is consistently spread over all point nodes in these composites, with phonon transport serving as the primary heat carriers, which originated from the BNP inclusion.

$$k_e = L_0 \sigma_e T \tag{24}$$

where L_0 is the Lorentz constant $\left(2.44 \times 10^{-8} \frac{W\Omega}{K^2}\right)$, k_e is the thermal conductivity due to electrons, σ_e is the electrical conductivity, and T is the temperature.[59]

Figure 14 displays the maximum magnitude of the nodal point temperatures, NT11, and the heat flux vector, HFL, for the RVE of BNP inclusions, the PEDOT:PSS matrix, and their nanocomposite under uniaxial macroscopic temperature gradient loading in the 1-, 2-, and 3-direction. Meanwhile, Figures S12–S14 show the distribution of the heat flow vector's magnitude, nodal point temperatures, and reaction flux for the inclusions, matrix, and nanocomposite along directions 1, 2, and 3. Also, Figures S15–S17 show the components of the heat flow vector, q_{11}, q_{22}, and q_{33}, for the inclusion of the matrix and nanocomposite along 1-, 2-, and 3-directions. For comparison, the thermal conductivity of several electrodes for energy storage is shown in Table 5.

According to the literature, the composite's thermal conductivity is decreased by the interfacial interactions between the polymer and nanofiller, which serve as a phonon scattering medium.[60] To account for the nanoeffects, particularly, interface thermal resistance (Kapitza resistance), the BNP was coated with an interphase to generate an effective filler having the same volume fraction as that of the BNP inclusion (Figure 15). Then, FE simulation was performed with the same data for the optimized electrode, and the result is presented in Table 4. After that, the general Maxwell–Garnett type effective medium approximation method (eqs 25 and 26) was adopted to compute the Kapitza effect from the effective thermal conductivity with the nanoeffect. The equation is said to compare favorably with experimental data for composites with low volume fractions, but the accuracy decreases for composites with higher volume fractions. For instance, as the volume percentage approaches a value of 30%, their estimated effective thermal conductivity deviates by nearly 50%.[61]

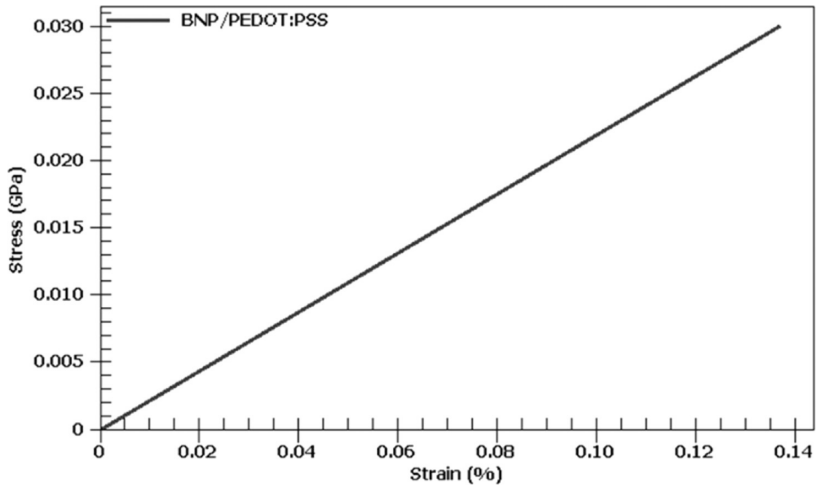

Figure 11. Stress–strain curve of the optimized BNP/PP nanocomposite.

https://doi.org/10.1021/acsomega.2c06716
ACS Omega 2022, 7, 48447–48466

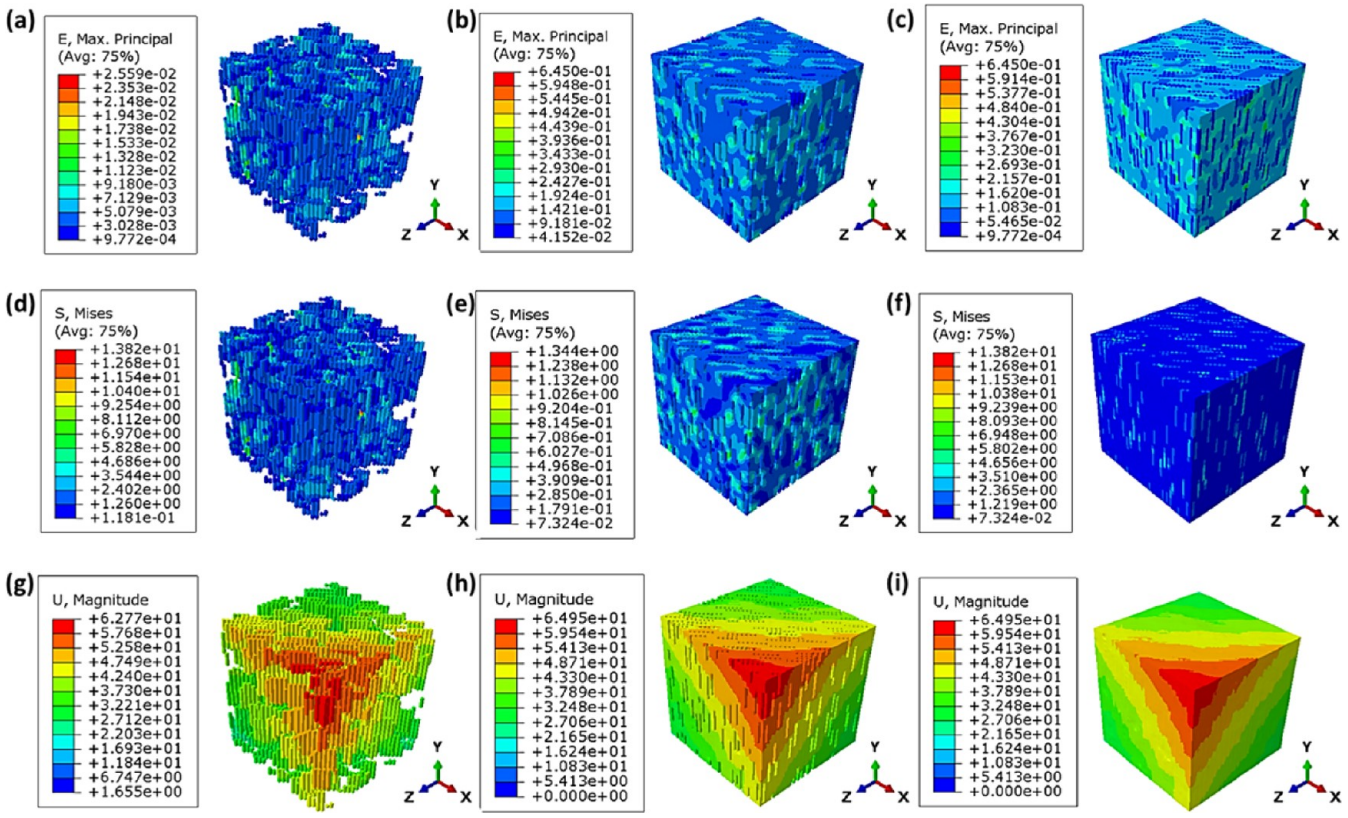

Figure 12. Maximum principal strain (first row), von Mises stress (second row), and displacement (third row) distribution under general 3D loading for the RVE of (a,d,g) BNP inclusions, (b,e,h) PEDOT:PSS matrix, and (c,f,i) nanocomposite of PEDOT:PSS/BNP.

Table 3. FE Homogenization Technique and RSM Prediction of the Effective Electrical Conductivity of the Optimal PEDOT:PSS/BNP Nanocomposite

	effective electrical conductivity					
	FE (S/cm)					
s/n	G_{11}	G_{22}	G_{33}	average	RSM (S/cm)	error (%)
1	606.29	646.24	605.73	619.42	633.85	2.33

$$K_{11}^{*} = K_{22}^{*} = K_{m}\frac{2 + f[\beta_{11}(1 - L_{11})(1 + \langle\cos^2 \emptyset\rangle) + \beta_{33}(1 - L_{33})(1 - \langle\cos^2 \emptyset\rangle)]}{2 + f[\beta_{11}L_{11}(1 + \langle\cos^2 \emptyset\rangle) + \beta_{33}L_{33}(1 - \langle\cos^2 \emptyset\rangle)]} \quad (25)$$

$$K_{33}^{*} = K_{m}\frac{1 + f[\beta_{11}(1 - L_{11})(1 + \langle\cos^2 \emptyset\rangle) + \beta_{33}(1 - L_{33})\langle\cos^2 \emptyset\rangle]}{1 + f[\beta_{11}L_{11}(1 + \langle\cos^2 \emptyset\rangle) + \beta_{33}L_{33}\langle\cos^2 \emptyset\rangle]} \quad (26)$$

$$\langle\cos^2 \emptyset\rangle = \frac{\int \rho(\emptyset)\ \cos^2 \emptyset\ \sin\ \emptyset\ d\emptyset}{\int \rho(\emptyset)\ \sin\ \emptyset\ d\emptyset} \quad (27)$$

For vertically aligned fillers, $\langle\cos^2 \emptyset\rangle = 0$, whereas for randomly oriented platelets, $\langle\cos^2 \emptyset\rangle = 1/3$, for platelets aligned at 45°, $\langle\cos^2 \emptyset\rangle = 1/2$, and for horizontally aligned fillers, $\langle\cos^2 \emptyset\rangle = 1$. Meanwhile, L_{ii} is a geometrical factor based on the shape of the inclusion, therefore, for the platelet.[62]

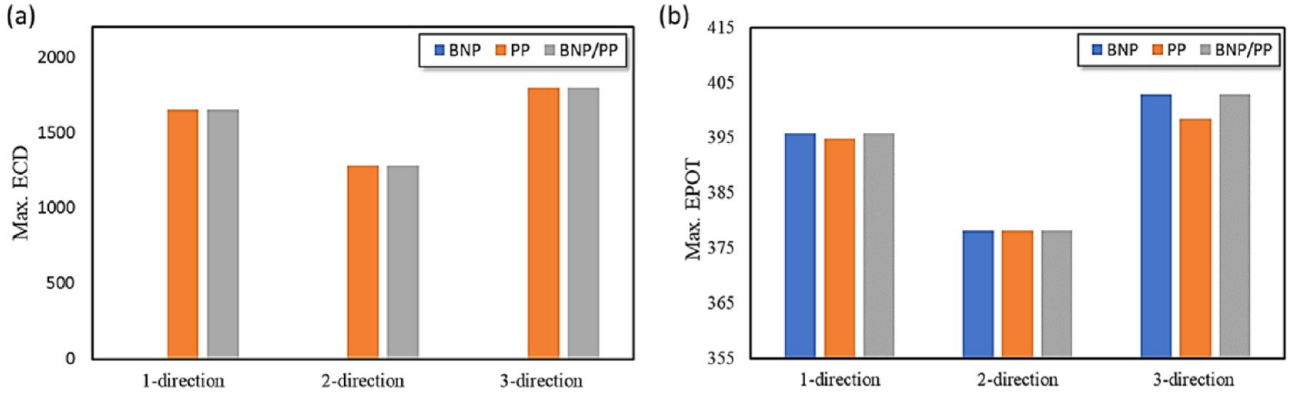

Figure 13. Histogram chart of the maximum magnitude of (a) ECD and (b) EPOT, under uniaxial macroscopic voltage gradient loading in the 1-, 2-, and 3-direction for the RVE of BNP inclusions, the PP matrix, and their nanocomposite.

https://doi.org/10.1021/acsomega.2c06716
ACS Omega 2022, 7, 48447−48466

Table 4. FE Homogenization Technique and RSM Prediction of the Effective Thermal Conductivities of the Optimal PEDOT/PSS/BNP Nanocomposite

	effective thermal conductivity						
	FE (W/m K)						
	K_{11}	K_{22}	K_{33}	average K	RSM (W/m K)	error (%)	average Kapitza resistance (10^{-9} m^2 K/W)
without the nanoeffect	1.91	2.73	1.28	1.97	1.96	0.6	
with the nanoeffect	2.10	4.22	1.54	2.62			
Kapitza resistance	2.42	2.42	2.42				2.42

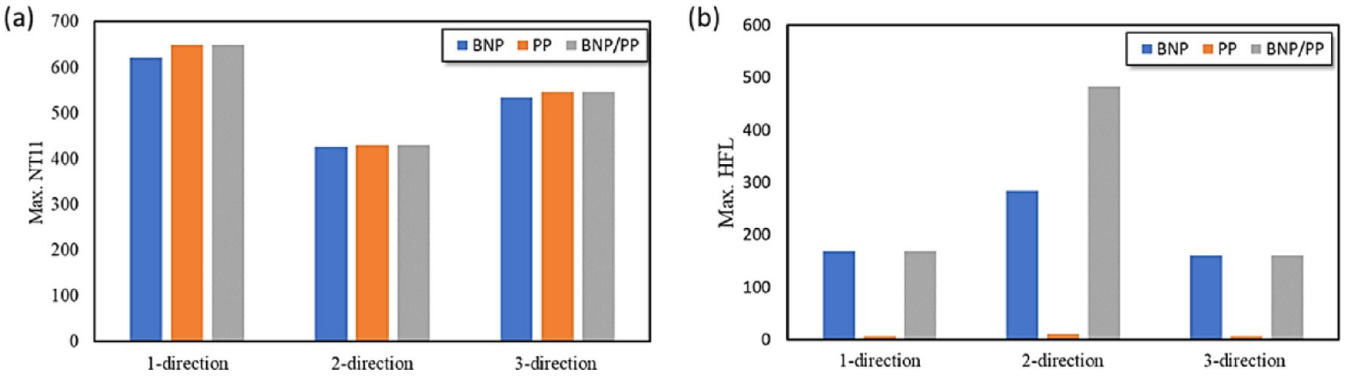

Figure 14. Histogram chart of the maximum magnitude of (a) nodal point temperatures, NT11 and (b) heat flux vector, HFL, under uniaxial macroscopic temperature gradient loading in the 1-, 2-, and 3-directions for the RVE of BNP inclusions, the PEDOT:PSS matrix, and their nanocomposite.

Table 5. Thermal Conductivity of Selected Electrodes

electrode	particle size (μm)	porosity (%)	K (W/m K)	refs
C	6−75		0.32−0.798	64
C			0.31 ± 0.05	65
NMC			0.14 ± 0.02	65
C			0.32 ± 0.03	66
LCO			0.17 ± 0.02	66
NMC			0.30 ± 0.05	66
LFP			0.13 ± 0.02	66
C	∼20	∼50	1.05	67
NMC	∼10	∼50	0.548	67
BNP/PP			1.96	in this work

$$L_{11} = L_{22} = \frac{P^2}{2(P^2 - 1)} - \frac{P}{2(1 - P^2)^{1.5}} \cos^{-1} p \quad (28)$$

$$L_{33} = 1 - 2L_{11} \quad (29)$$

BNP AR $p = d/t$, $d > t$

$$\beta_{ii} = \frac{K_{ii}^c - K_m}{K_m + L_{ii}(K_{ii}^c - K_m)} \quad (30)$$

$$K_{ii}^c = \frac{K_f}{\left(1 + \frac{\gamma L_{ii} K_f}{K_m}\right)} \quad (31)$$

$$\gamma = (1 + 2p)a_k \quad (32)$$

$$a_k = R_k K_m / t \quad (33)$$

where K_m and K_f are the thermal conductivities of the BNP and PP matrix, respectively, and K_{11}^*, K_{22}^*, and K_{33}^* are the components of effective thermal conductivities with nanoeffects. Meanwhile, f, d, and t are the volume fraction, diameter, and thickness of the BNP inclusion, respectively. Ø is the orientation angle of the platelet, $\rho(Ø)$ is the distribution function describing the orientation of the platelets, a_k is a dimensionless parameter

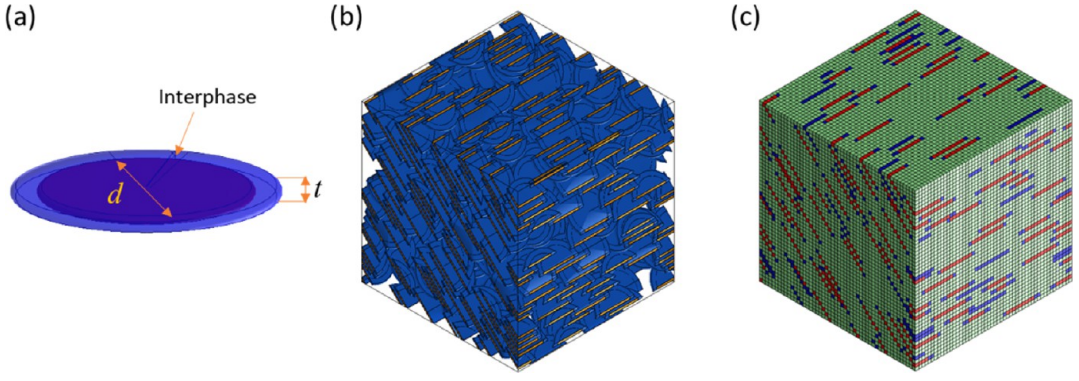

Figure 15. Schematic representation of (a) coated BNP (effective inclusion), (b) RVE of the effective BNP inclusion, and (c) RVE of the PEDOT:PSS/effective BNP nanocomposite.

https://doi.org/10.1021/acsomega.2c06716
ACS Omega 2022, 7, 48447−48466

describing the interfacial properties between the platelet and matrix, and R_k is the Kapitza resistance between the BNP inclusion and the PP matrix.[60−63] To simplify the calculation of the Kapitza resistance, the coating is assumed to have a constant thickness; therefore, K_m and K_f are assumed to be isotropic. As such, the computed interfacial thermal resistance of PP with the BNP is 2.42×10^{-9} m^2 K/W.

5. CONCLUSIONS

In this study, the properties of the PEDOT:PSS/BNP nanocomposite electrode were examined for BNP inclusions in the range of 1−25% volume ratio, 0.04−0.1 AR, and 45°, random, and 90° orientations. Therefore, based on the FE simulation results, the response variables of the transport and mechanical properties of the PEDOT:PSS/BNP nanocomposite were optimized using the RSM. First, RSM models were developed to predict the behavior of the nanocomposite accurately and confidently with 95% confidence. Then, the responses of the improved electrode parameters based on the desirability function were further predicted using the response surface. The predicted optimized nanocomposite with the desired properties for energy storage applications has a volume fraction of BNPs of 13.96%, an AR of 0.04, and an angle of 45°. The material's predicted Young's modulus is 6.73 GPa, its electrical conductivity is 633.85 S/cm, and its thermal conductivity is 1.96 W/m K, yielding a desirability value of 0.78 with a generally high prediction performance of <0.03 error. The interfacial thermal resistance computed from nanoeffect-based effective thermal conductivity of the nanocomposite is 2.42×10^{-9} m^2 K/W. The FE analysis of the optimized nanocomposite indicates that the BNP is the key factor in the reinforcement of the composite. At the same time, the electron transport of the conjugated double bonds along the PEDOT:PSS backbone chain dominates the electrical conductivity channel. The BNP phonon transport, however, is substantially responsible for the nanocomposite's heat flow. Based on these enhanced results, the optimized PEDOT:PSS/BNP nanocomposite electrode would serve as a promising material for the metal-ion battery. Therefore, further investigation is suggested to understand the storage capacity of the material for various metal-ion batteries. More importantly, since the BNP inclusion is a platelet, the electrode may be analyzed for thermal and electrical percolation studies as spherical, cylindrical, and sphero-cylindrical inclusions are the only types of inclusions that can be modeled using Digimat software for percolation studies. For further research of the mechanical properties of the electrode, it is suggested that PERMIX, an open-source software framework for multiscale modeling and simulation of fracture in solids, be used.[68]

ASSOCIATED CONTENT

Supporting Information

The Supporting Information is available free of charge at https://pubs.acs.org/doi/10.1021/acsomega.2c06716.

Data for the response surface design of the experiment; ANOVA and fit statistical result; frequency distribution of the FE data; 2D and 3D contour plots of the effects of the factors on the responses; and the distribution of the components and magnitude of displacement, ECD, EPOT, and heat flux vector (PDF)

AUTHOR INFORMATION

Corresponding Author

Suprakas Sinha Ray − *Centre for Nanostructures and Advanced Materials, DSI-CSIR Nanotechnology Innovation Centre, Council for Scientific and Industrial Research, CSIR, Pretoria 0001, South Africa; Department of Chemical Sciences, University of Johannesburg, Doornfontein 2028 Johannesburg, South Africa;* orcid.org/0000-0002-0007-2595; Email: rsuprakas@csir.co.za, ssinharay@uj.ac.za

Authors

Gbolahan Joseph Adekoya − *Institute of NanoEngineering Research (INER) & Department of Chemical, Metallurgical and Materials Engineering, Faculty of Engineering and the Built Environment, Tshwane University of Technology, Pretoria 0183, South Africa; Centre for Nanostructures and Advanced Materials, DSI-CSIR Nanotechnology Innovation Centre, Council for Scientific and Industrial Research, CSIR, Pretoria 0001, South Africa;* orcid.org/0000-0001-6381-0914

Oluwasegun Chijioke Adekoya − *Institute of NanoEngineering Research (INER) & Department of Chemical, Metallurgical and Materials Engineering, Faculty of Engineering and the Built Environment, Tshwane University of Technology, Pretoria 0183, South Africa;* orcid.org/0000-0002-5386-5919

Rotimi Emmanuel Sadiku − *Institute of NanoEngineering Research (INER) & Department of Chemical, Metallurgical and Materials Engineering, Faculty of Engineering and the Built Environment, Tshwane University of Technology, Pretoria 0183, South Africa*

Yskandar Hamam − *Department of Electrical Engineering, Faculty of Engineering and the Built Environment, Tshwane University of Technology, Pretoria 0183, South Africa; École Supérieure d'Ingénieurs en Électrotechnique et Électronique, Paris 93160, France*

Complete contact information is available at: https://pubs.acs.org/10.1021/acsomega.2c06716

Author Contributions

The manuscript was written with the contributions of all authors. G.J.A. and S.S.R. framed and organized the manuscript. O.C.A., Y.H., and R.E.S. edited and corrected.

Notes

The authors declare no competing financial interest.

ACKNOWLEDGMENTS

The G.B.J. would like to thank the National Research Foundation (Grant Number: 116083/138768) of South Africa for financial support. S.S.R. would like to thank the Department of Science and Innovation (grant no: C6ACH35) and the Council for Scientific and Industrial Research (grant no: 086ADMI) for financial support.

REFERENCES

(1) Xu, S.; Fan, Z.; Yang, S.; Zhao, Y.; Pan, L. Flexible, self-powered and multi-functional strain sensors comprising a hybrid of carbon nanocoils and conducting polymers. *Chem. Eng. J.* **2021**, *404*, 126064.
(2) Liu, F.; Xie, L.; Wang, L.; Chen, W.; Wei, W.; Chen, X.; Luo, S.; Dong, L.; Dai, Q.; Huang, Y.; Wang, L. Hierarchical Porous RGO/PEDOT/PANI Hybrid for Planar/Linear Supercapacitor with Outstanding Flexibility and Stability. *Nano-Micro Lett.* **2020**, *12*, 17.

(3) Adekoya, G. J.; Adekoya, O. C.; Sadiku, R. E.; Hamam, Y.; Ray, S. S. Applications of MXene-Containing Polypyrrole Nanocomposites in Electrochemical Energy Storage and Conversion. *ACS Omega* **2022**, *7*, 39498.
(4) Di Pierro, A.; Mortazavi, B.; Noori, H.; Rabczuk, T.; Fina, A. A Multiscale Investigation on the Thermal Transport in Polydimethylsiloxane Nanocomposites: Graphene vs. Borophene. *Nanomaterials* **2021**, *11*, 1252.
(5) Folorunso, O.; Hamam, Y.; Sadiku, R.; Ray, S. S.; Kumar, N. Investigation and modeling of the electrical conductivity of graphene nanoplatelets-loaded doped-polypyrrole. *Polym* **2021**, *13*, 1034.
(6) Kausar, A. Overview on conducting polymer in energy storage and energy conversion system. *J. Macromol. Sci., Part A: Pure Appl.Chem.* **2017**, *54*, 640−653.
(7) Chen, R.; He, H.; Hong, X. Z.; Le, Q.; Sun, K.; Ouyang, J. PEDOT:PSS as Stretchable Conductors with Good Wettability on the Substrate through the Simultaneous Plasticization and Secondary Doping with a Cationic or Anionic Surfactant. *Macromolecules* **2022**, *55*, 4967−4978.
(8) Zhang, L.; Yang, K.; Chen, R.; Zhou, Y.; Chen, S.; Zheng, Y.; Li, M.; Xu, C.; Tang, X.; Zang, Z.; et al. The Role of Mineral Acid Doping of PEDOT:PSS and Its Application in Organic Photovoltaics. *Adv. Electron. Mater.* **2020**, *6*, 1900648.
(9) Wang, C.; Sun, K.; Fu, J.; Chen, R.; Li, M.; Zang, Z.; Liu, X.; Li, B.; Gong, H.; Ouyang, J. Enhancement of Conductivity and Thermoelectric Property of PEDOT:PSS via Acid Doping and Single Post-Treatment for Flexible Power Generator. *Adv. Sustainable Syst.* **2018**, *2*, 1800085.
(10) Wu, F.; Li, P.; Sun, K.; Zhou, Y.; Chen, W.; Fu, J.; Li, M.; Lu, S.; Wei, D.; Tang, X.; et al. Conductivity Enhancement of PEDOT:PSS via Addition of Chloroplatinic Acid and Its Mechanism. *Adv. Electron. Mater.* **2017**, *3*, 1700047.
(11) Adekoya, G. J.; Sadiku, R. E.; Hamam, Y.; Ray, S. S.; Mwakikunga, B. W.; Folorunso, O.; Adekoya, O. C.; Lolu, O. J.; Biotidara, O. F. Pseudocapacitive material for energy storage application: PEDOT and PEDOT:PSS. *AIP Conf. Proc.* **2020**, *2289*, 020073.
(12) Sun, K.; Zhang, S.; Li, P.; Xia, Y.; Zhang, X.; Du, D.; Isikgor, F. H.; Ouyang, J. Review on application of PEDOTs and PEDOT:PSS in energy conversion and storage devices. *J. Mater. Sci.: Mater. Electron.* **2015**, *26*, 4438−4462.
(13) Adekoya, G. J.; Adekoya, O. C.; Sadiku, R. E.; Ray, S. S. Structure-property relationship and nascent applications of thermoelectric PEDOT:PSS/carbon composites: A review. *Compos. Commun.* **2021**, *27*, 100890.
(14) Huang, H.; Zhao, Y.; Cong, T.; Li, C.; Wen, N.; Zuo, X.; Guo, Y.; Zhang, H.; Fan, Z.; Pan, L. Flexible and Alternately Layered High-Loading Film Electrode based on 3D Carbon Nanocoils and PEDOT:PSS for High-Energy-Density Supercapacitor. *Adv. Funct. Mater.* **2022**, *32*, 2110777.
(15) Adekoya, G. J.; Sadiku, R. E.; Ray, S. S. Nanocomposites of PEDOT:PSS with Graphene and its Derivatives for Flexible Electronic Applications: A Review. *Macromol. Mater. Eng.* **2021**, *306*, 2000716.
(16) Varghese, K.; Baji, D. S.; Nair, S.; Santhanagopalan, D. Conducting polymer PEDOT:PSS coated Co3O4 nanoparticles as the anode for sodium-ion battery applications. *Front. Mater. Sci.* **2022**, *16*, 220601.
(17) Teng, W.; Zhou, Q.; Wang, X.; Gao, J.; Hu, P.; Du, Y.; Li, H.; Wang, J. Enhancing ions/electrons dual transport in rGO/PEDOT:PSS fiber for high-performance supercapacitor. *Carbon* **2022**, *189*, 284−292.
(18) Türkmen, T. A.; Taşaltın, N.; Taşaltın, C.; Baytemir, G.; Karakuş, S. PEDOT: PSS/β12 borophene nanocomposites as an inorganic-organic hybrid electrode for high performance supercapacitors. *Inorg. Chem. Commun.* **2022**, *139*, 109329.
(19) Arabha, S.; Akbarzadeh, A. H.; Rajabpour, A. Engineered porous borophene with tunable anisotropic properties. *Composites, Part B* **2020**, *200*, 108260.
(20) Mannix, A. J.; Zhou, X.-F.; Kiraly, B.; Wood, J. D.; Alducin, D.; Myers, B. D.; Liu, X.; Fisher, B. L.; Santiago, U.; Guest, J. R.; Yacaman, M. J.; Ponce, A.; Oganov, A. R.; Hersam, M. C.; Guisinger, N. P. Synthesis of borophenes: Anisotropic, two-dimensional boron polymorphs. *Science* **2015**, *350*, 1513.
(21) Peng, B.; Zhang, H.; Shao, H.; Xu, Y.; Zhang, R.; Zhu, H. The electronic, optical, and thermodynamic properties of borophene from first-principles calculations. *J. Mater. Chem. C* **2016**, *4*, 3592−3598.
(22) Kistanov, A. A.; Khadiullin, S. K.; Dmitriev, S. V.; Korznikova, E. A. Effect of oxygen doping on the stability and band structure of borophene nanoribbons. *Chem. Phys. Lett.* **2019**, *728*, 53−56.
(23) Kistanov, A. A.; Cai, Y.; Zhou, K.; Srikanth, N.; Dmitriev, S. V.; Zhang, Y.-W. Exploring the charge localization and band gap opening of borophene: a first-principles study. *Nanoscale* **2018**, *10*, 1403−1410.
(24) Penev, E. S.; Kutana, A.; Yakobson, B. I. Can Two-Dimensional Boron Superconduct? *Nano Lett.* **2016**, *16*, 2522−2526.
(25) Jiang, H. R.; Lu, Z.; Wu, M. C.; Ciucci, F.; Zhao, T. S. Borophene: A promising anode material offering high specific capacity and high rate capability for lithium-ion batteries. *Nano Energy* **2016**, *23*, 97−104.
(26) Yin, Y.; Hu, Y.; Li, S.; Ding, G.; Wang, S.; Li, D.; Zhang, G. Abnormal thermal conductivity enhancement in covalently bonded bilayer borophene allotrope. *Nano Res.* **2022**, *15*, 3818−3824.
(27) Tian, W.; Qi, L.; Chao, X.; Liang, J.; Fu, M. W. Numerical evaluation on the effective thermal conductivity of the composites with discontinuous inclusions: Periodic boundary condition and its numerical algorithm. *Int. J. Heat Mass Transfer* **2019**, *134*, 735−751.
(28) Pal, R. On the Lewis-Nielsen model for thermal/electrical conductivity of composites. *Composites, Part A* **2008**, *39*, 718−726.
(29) Ali, D.; Sen, S. Finite element analysis of the effect of boron nitride nanotubes in beta tricalcium phosphate and hydroxyapatite elastic modulus using the RVE model. *Composites, Part B* **2016**, *90*, 336−340.
(30) Adekoya, G. J.; Adekoya, O. C.; Sadiku, E. R.; Hamam, Y.; Ray, S. S. Effect of Borophene and Graphene on the Elastic Modulus of PEDOT:PSS Film-A Finite Element Study. *Condens. Matter* **2022**, *7*, 22.
(31) David Müzel, S.; Bonhin, E. P.; Guimarães, N. M.; Guidi, E. S. Application of the Finite Element Method in the Analysis of Composite Materials: A Review. *Polymers* **2020**, *12*, 818.
(32) Beluch, W.; Hatłas, M. Response surfaces in the numerical homogenization of nonlinear porous materials. *Eng. Trans.* **2019**, *67*, 213−226.
(33) Niu, J.; Wang, Z.; An, X.; Ma, B.; Liu, H.; Ma, Y.; Jiang, P.; Wang, Y.; Pang, H.; Wang, X. Response surface optimization and finite element simulation to prepare microporous carbon refractories via cold isostatic pressing. *Powder Technol.* **2022**, *398*, 117060.
(34) Gharaibeh, M. A.; Tlilan, H.; Gharaibeh, B. M. Y. Stress concentration factor analysis of countersunk holes using finite element analysis and response surface methodology. *Aust. J. Mech. Eng.* **2021**, *19*, 30−38.
(35) Qu, M.; Nilsson, F.; Qin, Y.; Yang, G.; Gao, Q.; Xu, W.; Liu, X.; Schubert, D. W. Electrical conductivity of anisotropic PMMA composite filaments with aligned carbon fibers - predicting the influence of measurement direction. *RSC Adv.* **2020**, *10*, 4156−4165.
(36) Amirmaleki, M.; Samei, J.; Green, D. E.; van Riemsdijk, I.; Stewart, L. 3D micromechanical modeling of dual phase steels using the representative volume element method. *Mech. Mater.* **2016**, *101*, 27−39.
(37) Tian, W.; Qi, L.; Chao, X.; Liang, J.; Fu, M. Periodic boundary condition and its numerical implementation algorithm for the evaluation of effective mechanical properties of the composites with complicated micro-structures. *Composites, Part B* **2019**, *162*, 1−10.
(38) e-xstream. *Digimat-A nonlinear multiscale material modeling platform*; e-xstream: ZAE Robert Steichen—5 rue Bommel Hautcharage, L-4940, Luxembourg, 2017.
(39) Trzepieciński, T.; Ryzińska, G.; Biglar, M.; Gromada, M. Modelling of multilayer actuator layers by homogenization technique using Digimat software. *Ceram. Int.* **2017**, *43*, 3259−3266.

https://doi.org/10.1021/acsomega.2c06716
ACS Omega 2022, 7, 48447−48466

(40) Ou, M.; Wang, X.; Yu, L.; Liu, C.; Tao, W.; Ji, X.; Mei, L. The Emergence and Evolution of Borophene. *Adv. Sci.* **2021**, *8*, 2001801.
(41) Lenz, A.; Kariis, H.; Pohl, A.; Persson, P.; Ojamäe, L. The electronic structure and reflectivity of PEDOT:PSS from density functional theory. *Chem. Phys.* **2011**, *384*, 44−51.
(42) Kyaw, A. K. K.; Yemata, T. A.; Wang, X.; Lim, S. L.; Chin, W. S.; Hippalgaonkar, K.; Xu, J. Enhanced Thermoelectric Performance of PEDOT:PSS Films by Sequential Post-Treatment with Formamide. *Macromol. Mater. Eng.* **2018**, *303*, 1700429.
(43) Liu, J.; Wang, X.; Li, D.; Coates, N. E.; Segalman, R. A.; Cahill, D. G. Thermal Conductivity and Elastic Constants of PEDOT:PSS with High Electrical Conductivity. *Macromolecules* **2015**, *48*, 585−591.
(44) Lee, M.; Jang, Y.; Oh, J.; Jung, J. A silver-nanoparticle-embedded activated-carbon−PEDOT:PSS composite conductor for enhancing electrical conductivity of a gas sensor module. *Dig. J. Nanomater. Bios.* **2018**, *13*, 527−534.
(45) Zeng, Y.; Chalise, D.; Lubner, S. D.; Kaur, S.; Prasher, R. S. A review of thermal physics and management inside lithium-ion batteries for high energy density and fast charging. *Energy Storage Mater.* **2021**, *41*, 264−288.
(46) Bernardin, C.; Olla, S. Fourier's law for a microscopic model of heat conduction. *J. Stat. Phys.* **2005**, *121*, 271−289.
(47) Mortazavi, B.; Bardon, J.; Ahzi, S. Interphase effect on the elastic and thermal conductivity response of polymer nanocomposite materials: 3D finite element study. *Comput. Mater. Sci.* **2013**, *69*, 100−106.
(48) Kleijnen, J. P. C. Kriging metamodeling in simulation: A review. *Eur. J. Oper. Res.* **2009**, *192*, 707−716.
(49) Jensen, W. A. Response Surface Methodology: Process and Product Optimization Using Designed Experiments 4th edition. *J. Qual. Technol.* **2017**, *49*, 186.
(50) Dar, F. H.; Meakin, J. R.; Aspden, R. M. Statistical methods in finite element analysis. *J. Biomech.* **2002**, *35*, 1155−1161.
(51) Subasi, A.; Sahin, B.; Kaymaz, I. Multi-objective optimization of a honeycomb heat sink using Response Surface Method. *Int. J. Heat Mass Transfer* **2016**, *101*, 295−302.
(52) Memon, A. M.; Hartadi Sutanto, M.; Napiah, M.; Khan, M. I.; Rafiq, W. Modeling and optimization of mixing conditions for petroleum sludge modified bitumen using response surface methodology. *Constr. Build. Mater.* **2020**, *264*, 120701.
(53) Mohammed, B. S.; Khed, V. C.; Nuruddin, M. F. Rubbercrete mixture optimization using response surface methodology. *J. Cleaner Prod.* **2018**, *171*, 1605−1621.
(54) Lai, J.; Wang, H.; Wang, D.; Fang, F.; Wang, F.; Wu, T. Ultrasonic Extraction of Antioxidants from Chinese Sumac (Rhus typhina L.) Fruit Using Response Surface Methodology and Their Characterization. *Molecules* **2014**, *19*, 9019−9032.
(55) Wang, X.; Wang, Z.; Wu, G.; Gan, J.; Yang, Y.; Huang, H.; He, J.; Zhong, H. Combining the finite element method and response surface methodology for optimization of shot peening parameters. *Int. J. Fatigue* **2019**, *129*, 105231.
(56) Jeong, I.-J.; Kim, K.-J. D-STEM: a modified step method with desirability function concept. *Comput. Oper. Res.* **2005**, *32*, 3175−3190.
(57) Derringer, G.; Suich, R. Simultaneous optimization of several response variables. *J. Qual. Technol.* **1980**, *12*, 214−219.
(58) Ashenai Ghasemi, F.; Daneshpayeh, S.; Ghasemi, I.; Ayaz, M. An investigation on the Young's modulus and impact strength of nanocomposites based on polypropylene/linear low-density polyethylene/titan dioxide (PP/LLDPE/TiO_2) using response surface methodology. *Polym. Bull.* **2016**, *73*, 1741−1760.
(59) Tarhini, A.; Alchamaa, M. W.; Khraiche, M.; Kazan, M.; Tehrani-Bagha, A. The effect of temperature on the electrical and thermal conductivity of graphene-based polymer composite films. *J. Appl. Polym. Sci.* **2022**, *139*, 51896.
(60) Dunn, M. L.; Taya, M. The effective thermal conductivity of composites with coated reinforcement and the application to imperfect interfaces. *J. Appl. Phys.* **1993**, *73*, 1711−1722.
(61) He, B.; Mortazavi, B.; Zhuang, X.; Rabczuk, T. Modeling Kapitza resistance of two-phase composite material. *Compos. Struct.* **2016**, *152*, 939−946.
(62) Lin, Z.; Liu, Y.; Raghavan, S.; Moon, K.-s.; Sitaraman, S. K.; Wong, C.-p. Magnetic Alignment of Hexagonal Boron Nitride Platelets in Polymer Matrix: Toward High Performance Anisotropic Polymer Composites for Electronic Encapsulation. *ACS Appl. Mater. Interfaces* **2013**, *5*, 7633−7640.
(63) Every, A. G.; Tzou, Y.; Hasselman, D. P. H.; Raj, R. The effect of particle size on the thermal conductivity of ZnS/diamond composites. *Acta Ichthyol. Piscatoria* **1992**, *40*, 123−129.
(64) Maleki, H.; Selman, J. R.; Dinwiddie, R. B.; Wang, H. High thermal conductivity negative electrode material for lithium-ion batteries. *J. Power Sources* **2001**, *94*, 26−35.
(65) Richter, F.; Vie, P. J. S.; Kjelstrup, S.; Burheim, O. S. Measurements of ageing and thermal conductivity in a secondary NMC-hard carbon Li-ion battery and the impact on internal temperature profiles. *Electrochim. Acta* **2017**, *250*, 228−237.
(66) Richter, F.; Kjelstrup, S.; Vie, P. J. S.; Burheim, O. S. Thermal conductivity and internal temperature profiles of Li-ion secondary batteries. *J. Power Sources* **2017**, *359*, 592−600.
(67) Lubner, S. D.; Kaur, S.; Fu, Y.; Battaglia, V.; Prasher, R. S. Identification and characterization of the dominant thermal resistance in lithium-ion batteries using operando 3-omega sensors. *J. Appl. Phys.* **2020**, *127*, 105104.
(68) Talebi, H.; Silani, M.; Bordas, S. P. A.; Kerfriden, P.; Rabczuk, T. A computational library for multiscale modeling of material failure. *Comput. Mech.* **2014**, *53*, 1047−1071.

https://doi.org/10.1021/acsomega.2c06716
ACS Omega 2022, 7, 48447−48466